Hot wire and PIV studies of transonic turbulent wall-bounded flows

by

Timmy Sigfrids

Till Mamma ...

... och Pappa

Timmy Sigfrids 2003 Hot wire and PIV studies of transonic turbulent wall-bounded flows

Department of Mechanics, Royal Institute of Technology
S-100 44 Stockholm, Sweden

Abstract

The compressible turbulent boundary layer developing over a two-dimensional bump which leads to a supersonic pocket with a terminating shock wave has been studied. The measurements have been made with hot-wire anemometry and Particle Image Velocimetry (PIV).

A method to calibrate hot-wire probes in compressible flow has been developed which take into account not only the flow velocity but also the influence of the Mach number, stagnation temperature and fluid density. The calibration unit consists of a small jet flow facility, where the temperature can be varied. The hot wires are calibrated in the potential core of the free jet. The jet emanates in a container where the static pressure can be controlled, and thereby the gas density. The calibration method was verfied in the flat plate zero pressure gradient turbulent boundary layer in front of the bump at three different Mach numbers, namely 0.3, 0.5 and 0.7. The profiles were also measured at different static pressures in order to see the influence of varying density. Good agreement between the profiles measured at different pressures, as well as with the standard logarithmic profile was obtained.

The PIV measurements of the boundary layer flow in front of the 2D bump showed good agreement with the velocity profiles measured with hot-wire anemometry. The shock wave boundary layer interaction was investigated for an inlet Mach number of 0.69. A lambda shock wave was seen on the downstream side of the bump. The velocity on both sides of the shock wave as measured with the PIV was in good agreement with theory. The shock wave was found to cause boundary layer separation, which was seen as a rapid growth of the boundary layer thickness downstream the shock. However, no back flow was seen in the PIV-data, probably because the seeding did not give enough particles in the separated region. The PIV data also showed that the shock wave was oscillating, *i.e.* it was moving approximately 5 mm back and forth. This distance corresponds to about five boundary layer thicknesses in terms of the boundary layer upstream the shock.

Parts of this work has been presented at:

STEM group conference, 14-15 September 2000 *Älvkarleby, Sweden*
The Swedish mechanics days, 11-13 June 2001 *Linköping, Sweden*
STEM group conference, 27 June 2001 *Stockholm, Sweden*
ERCOFTAC NPC, 29-30 August 2001 *Magleås, Denmark*
ETC 9, 2-5 July 2002 *Southampton, U.K.*
STEM/CECOST group conference, 5-7 November 2002 *Lund, Sweden*

Contents

CONTENTS

CHAPTER 1

Introduction

With a viscous fluid (gas or liquid) in relative motion to a surface, a boundary layer will form. At the surface the fluid will have the same velocity as the surface itself (no-slip condition) and will with increasing distance from the surface gradually approach the velocity of the fluid far away from the surface. The flow in the boundary layer can be classified either as laminar or turbulent and the type of flow is for a specific geometry determined by the Reynolds number, the ratio of the viscous forces and the inertia forces, where sufficiently high Reynolds numbers give turbulent flow. For an intermediate Reynolds number range both laminar and turbulent flow may occur together and the flow is then denoted transitional.

In many engineering applications with gas flow the flow reaches such high velocities that the resulting pressure variations give rise to large changes in the gas density. Such flows are denoted compressible. This is for instance the case when the relative speed between an object and the fluid outside the boundary layer is higher than the speed of sound. In such a case the flow is supersonic, whereas if the flow speed everywhere is lower than the speed of sound it is denoted subsonic. However, even a subsonic flow must be viewed as compressible if the Mach number (the ratio of the flow velocity and the speed of sound) is larger than approximately 0.3.

Even though the approaching free stream velocity is subsonic the flow can be accelerated over a body surface and regions where the speed is supersonic may develop. Such a flow field is usually called transonic. A definition of transonic flow suggested by Shapiro (1954) is: A flow containing both subsonic and supersonic velocities. Transonic flow is typically in the Mach number range 0.7 to 1.3. In a boundary layer, there will always be a region close to the surface where the flow velocity will be less than the speed of sound, even though the free stream is supersonic. Despite of this, boundary layer flows are not in themselves denoted transonic flows.

Transonic flows can typically be found over aircraft wings since commercial transport planes usually operate in the transonic speed regime. The flow over helicopter rotors and propellers in high speed flight also often becomes transonic. Turbomachinery components such as compressors and turbines are designed to operate at transonic speeds. A poorly designed component operating in transonic flow may cause a strong shock wave that cause boundary layer separation and leads to loss of lift and increase in drag.

1. INTRODUCTION

An illustration of the behaviour of the flow over a wing profile at transonic speeds can be found in figure 1.1. In figure 1.1(a), the freestream Mach number has a supercritical value, *i.e.* the local Mach number has reached unity at some point and a pocket of supersonic flow exists which is terminated by a shock wave.
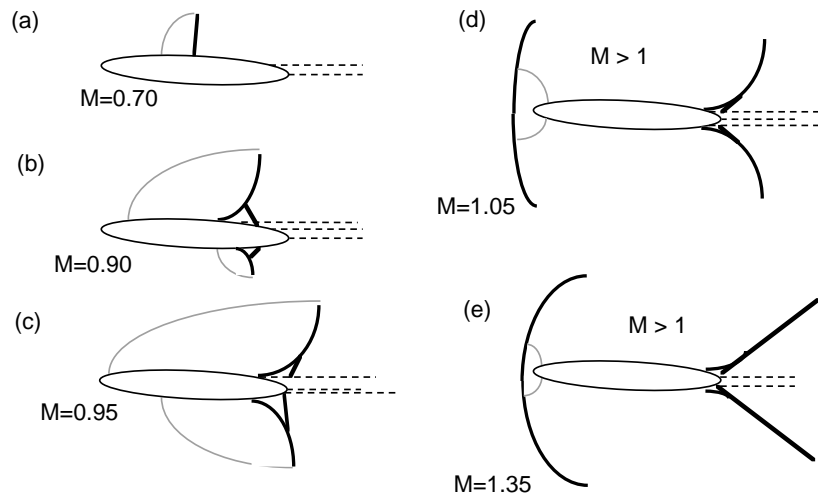

FIGURE 1.1. Flow patterns for transonic flow over a wing profile at a small angle of attack. The grey curves are the sonic line, *i.e.* the line where M=1. The dashed lines mark separated flow.

As the free-stream Mach number increases, the shock wave moves rearward and the supersonic pocket increases in size as shown in figure 1.1(b). Ultimately, the shock becomes so strong that, as a result of the shock wave boundary layer interaction, separation occurs, and the shock wave forms a lambda pattern. The separation is marked with the dashed lines.

Figure 1.1(c) shows a higher free-stream Mach number where the shock is moved towards the tail of the wing profile and becomes stronger. The flow over the surface of the wing is mainly supersonic except near the nose. When the speed reaches a value just above sonic, the flow is similar to that of a flow with a Mach number slightly below 1. The main difference is that a detached shock can be found upstream of the nose of the wing profile, as shown in figure 1.1(d).

Figure 1.1(e) shows a typical pattern close to the attachment of the shock to the leading edge of the wing profile. The subsonic region close to the nose becomes smaller and the shock at the end of the wing profile is sharper. The flow pattern is similar to that of flow across sharp edged profiles, such as a wedge.

Despite the importance of the transonic flow regime there is still a lack of fundamental understanding of the physics of the boundary layer in transonic flow and especially the interaction between the boundary layer and the shock wave. This lack of basic understanding of the transonic flow are due to both experimental and theoretical difficulties in studying such flows. For instance the equations of motion that describe the flow have two different characteristics, elliptic or hyperbolic, depending on whether the flow is subsonic or supersonic. In a transonic flow both regions exist simultaneously which make theoretical and numerical approaches complicated.

Experiments in transonic flows also give rise to problems that are less severe in subsonic and supersonic flows. For instance disturbances from a model propagates almost normal to the flow direction and are reflected from the wind tunnel walls towards the model. The flow field is also in general quite sensitive to disturbances, which is a problem when intrusive measuring methods such as hot-wire anemometry are used. Hot wires are also subjected to high rates of strain caused by the high dynamic pressure. Another difficulty with hot-wire anemometry is that the method is based on the heat transfer between the flow and the probe and that in compressible flow the heat transfer is not only a function of the velocity but also dependent on the density, Mach number and temperature.

Because of the problems encountered with hot-wires, non-intrusive optical methods may be preferable to use. Both schlieren optics, where density gradients in the flow are registered, or methods which use small tracer particles can been used. Laser Doppler Velocimetry (LDV) and Particle Image Velocimetry (PIV) belong to techniques which register the speed of trace particles. However it is important that the particles introduced in the flow field follow the flow accurately in order to obtain correct results. For high speed flows this severely limits the size of usable particles. One disadvantage with these methods as compared to hot-wire anemometry is that the flow field cannot be time resolved.

1.1. The scope of the thesis

In this thesis wall-bounded turbulent flows at subsonic, but compressible flow conditions are investigated experimentally in a wind tunnel. Both the incoming turbulent boundary layer along the wind tunnel wall, as well as the complicated flow field above a two-dimensional wall bumb, with a supersonic pocket and a terminating shock, are investigated. The thesis is organized as follows. Chapter 2 gives an introduction to the theory of both laminar and turbulent boundary layers under compressible flow conditions as well as a discussion of phenomena related to shock wave/boundary layer interaction. Chapter 3 gives a brief description of the wind-tunnel and experimental set-up, as well as a description of the PIV technique. The basics of hot-wire anemometry for compressible flows as well as a calibration technique are described in some detail in

chapter 4. The boundary layer results obtained both with hot-wire anemometry and PIV are given in chapter 5, and finally chapter 6 summarises the results found.

Compressible boundary layer theory

2.1. Equations of motion for compressible flow

The most important non-dimensional parameters in compressible flows are the Reynolds number,

$$Re = \frac{\rho U L}{\mu}, \tag{2.1}$$

the Mach number

$$M = \frac{U_\infty}{\sqrt{\gamma R T_\infty}}, \tag{2.2}$$

and the Prandtl number,

$$Pr = \frac{\mu}{\rho \alpha}, \tag{2.3}$$

where U and L are the characteristic velocity and length, ρ and μ are the density and dynamic viscosity, γ is the ratio between the specific heats, R is the specific gas constant, T is the temperature and α the thermal diffusivity.

The equations of motion for a compressible, viscous, heat conducting fluid are:
the continuity equation:

$$\frac{\partial \rho}{\partial t} + \frac{\partial \rho u_i}{\partial x_i} = 0, \tag{2.4}$$

the momentum equation:

$$\rho(\frac{\partial u_i}{\partial t} + u_j \frac{\partial u_i}{\partial x_j}) = -\frac{\partial p}{\partial x_i} + \frac{\partial d_{ij}}{\partial x_j}, \tag{2.5}$$

where the deviatoric stress tensor d_{ij} is given by:

$$d_{ij} = \mu \left(\frac{\partial u_i}{\partial x_j} + \frac{\partial u_j}{\partial x_i} - \frac{2}{3} \frac{\partial u_k}{\partial x_k} \delta_{ij} \right), \tag{2.6}$$

and the energy equation:

$$\rho(\frac{\partial h}{\partial t} + u_j \frac{\partial h}{\partial x_j}) = \frac{\partial p}{\partial t} + u_j \frac{\partial p}{\partial x_j} - \frac{\partial}{\partial x_i} \left(k \frac{\partial T}{\partial x_i} \right) + d_{ij} \frac{\partial u_i}{\partial x_j}. \tag{2.7}$$

where h is the enthalpy, defined as $dh = c_p dT$, and c_p is the specific heat of the gas at constant pressure. Using the perfect gas law, the entalphy can be written more conveniently as:

$$h = e + \frac{p}{\rho}, \tag{2.8}$$

with e as the internal energy, and the stagnation enthalpy,

$$h_0 = h + \frac{1}{2}V^2. \tag{2.9}$$

where $V^2 = u_i u_i$. The variation of dynamic viscosity, μ, with temperature can be described with Sutherland's formula, valid in the temperature range of 100 K and 1900 K,

$$\frac{\mu}{\mu_0} = \frac{T_0 + S_0}{T + S_0}, \left(\frac{T}{T_0}\right)^{3/2}. \tag{2.10}$$

where S_0=110.3 K. Including the perfect gas law,

$$p = \rho R T, \tag{2.11}$$

and knowning the variation of viscosity and thermal conductivity (or the Prandtl number) with temperature and pressure, the above equations are a closed set, describing compressible fluid flow. The assumptions that have been made can be summarized as:

- the continuum hypothesis holds,
- the fluid particles are in local thermodynamic equilibrium,
- body forces can be neglected,
- the fluid is Newtonian,
- heat conduction follows Fourier's law,
- radiative heat transfer can be neglected.

The boundary conditions for the velocity at a wall is the no-slip condition for the velocity, *i.e.* the velocity at the wall is the same as that of the wall itself. For the temperature the boundary condition depends on the type of wall, for instance whether the wall is adiabatic (*i.e.* no heat transfer from the fluid to the wall) or if it is a constant temperature wall.

2.2. Laminar boundary layers

2.2.1. *Boundary layer equations for compressible flow*

The boundary layer equations are obtained assuming stationarity and that variations in the streamwise (x) direction are much slower than in the wall normal (y) direction. For a two-dimensional boundary layer eqs. (2.4), (2.5) and (2.7) reduce to

$$\frac{\partial(\rho u)}{\partial x} + \frac{\partial(\rho v)}{\partial y} = 0 \tag{2.12}$$

$$\rho \left(u\frac{\partial u}{\partial x} + v\frac{\partial u}{\partial y} \right) = -\frac{\partial p}{\partial x} + \frac{\partial}{\partial y}\left(\mu\frac{\partial u}{\partial y} \right) \tag{2.13}$$

$$\frac{\partial p}{\partial y} = 0 \tag{2.14}$$

$$\rho \left(u\frac{\partial h}{\partial x} + v\frac{\partial h}{\partial y} \right) = u\frac{\partial p}{\partial x} + \frac{\partial}{\partial y}\left(k\frac{\partial T}{\partial y} \right) + \mu\left(\frac{\partial u}{\partial y} \right)^2 \tag{2.15}$$

These equations have to be complemented with suitable boundary conditions which will be discussed later.

Some important boundary layer parameters are the displacement thickness, the momentum loss thickness and the shape factor. The displacement thickness, δ^*, is the distance the streamlines of the outer flow are displaced by the boundary layer,

$$\delta^* = \int_0^\delta \left(1 - \frac{\rho u}{\rho_\infty U_\infty} \right) \mathrm{d}y. \tag{2.16}$$

The momentum loss thickness represents the momentum loss due to the existense of the boundary layer.

$$\theta = \int_0^\delta \frac{\rho u}{\rho_\infty U_\infty}\left(1 - \frac{u}{U_\infty} \right) \mathrm{d}y \tag{2.17}$$

whereas the shape factor

$$H = \frac{\delta^*}{\theta} \tag{2.18}$$

characterizes the shape of the mean velocity (and density) profile.

The parameters are here defined for compressible flow but can be reduced to the incompressible ones in the limit of a constant density distribution over the boundary layer, $i.e.$ $\rho = \rho_\infty$.

2.2.2. Blasius similarity solution

Assuming incompressible, laminar flow the boundary layer equations can be written as

$$f''' + \frac{1}{2}ff'' = 0, \tag{2.19}$$

with the the streamwise velocity proportional to the first derivative of the function f with the free-stream velocity as the proportionality constant,

$$u = f'(\eta)U_\infty, \tag{2.20}$$

and η is a similarity coordinate

$$\eta = y\sqrt{\frac{U_\infty}{\nu x}}. \tag{2.21}$$

2. COMPRESSIBLE BOUNDARY LAYER THEORY

The normal velocity v is

$$v = \frac{1}{2}\sqrt{\frac{\nu U_\infty}{x}}\left[\eta f'(\eta) - f(\eta)\right]. \tag{2.22}$$

The boundary conditions at the wall for equation (2.19), are the no-slip condition for u and zero normal velocity at the impermeable wall, $v = 0$, whereas far from the wall the streamwise velocity should reach the free-stream value:

$$\begin{cases} u(y = 0) = 0 & \Rightarrow & f'(\eta = 0) = 0 \\ v(y = 0) = 0 & \Rightarrow & f(\eta = 0) = 0 \\ u(y \to \infty) = U_\infty & \Rightarrow & f'(\eta \to \infty) = 1 \end{cases} \tag{2.23}$$

With the boundary conditions above, eq. (2.19), can be solved with for instance a shooting method. This solution is called the *Blasius solution*.

For incompressible flow when the assumption of constant density is applicable, the definitions for the displacement thickness, eq. (2.16) and the momentum loss thickness, eq. (2.17) are reduced to expressions which are only velocity dependent. With the Blasius solution the shape factor, eq. (2.18), can be determined to be $H = 2.59$.

2.2.3. *The Howarth-Dorodnitzyn transformation*

The Howarth-Dorodnitzyn transformation can be used to reduce the compressible boundary layer equations to the Blasius boundary layer equation by transforming the coordinates so that the unknown density distribution is incorporated in a transformed variable. The temperature equation can also be transformed and then written as an ordinary differential equation (ODE) with variable coefficients which are given by the Blasius solution. The normal coordinate is transformed as:

$$y_{HD} = \int_0^y \frac{\rho(x,y)}{\rho_\infty}\mathrm{d}y, \tag{2.24}$$

and the similarity variable is

$$\eta = y_{HD}\sqrt{\frac{\rho_\infty U_\infty}{\mu_\infty x}}, \tag{2.25}$$

whereas the streamwise velocity is still described as $u = U_\infty f'(\eta)$.

With the above expressions the x-momentum equation is reduced to the Blasius equation (2.19), with the same boundary conditions, eq. (2.23), and can be solved in the same way.

Introducing a non-dimensional temperature function as

$$\frac{T}{T_\infty} = \Theta_{HD}(\eta), \tag{2.26}$$

then the energy equation can be transformed in the same way as the x-momentum equation. This gives

$$\Theta''_{HD} + \frac{Pr}{2}f\Theta'_{HD} + Pr(\gamma - 1)M_\infty^2 f''^2 = 0, \tag{2.27}$$

8

which is an ODE and can easily be solved if the solution to the Blasius equation is known. For $Pr = 1$ an analytical solution can be found, with the boundary conditions

$$\begin{cases} \Theta_{HD}(\eta = 0) = \Theta_w & \text{and} \quad f'(\eta = 0) = 0 \\ \Theta_{HD}(\eta \to \infty) = 1 & \text{and} \quad f'(\eta \to \infty) = 1. \end{cases} \tag{2.28}$$

The solution for the temperature is

$$\Theta_{HD} = \Theta_w + (1 - \Theta_w)f' + \frac{1}{2}(\gamma - 1)M_\infty^2(f' - f'^2). \tag{2.29}$$

For a Prandtl number close to one it has been shown (see for instance Schlichting & Gersten (1996)) that an approximation of the temperature distribution can be written as

$$\Theta_{HD} = \Theta_w + (1 - \Theta_w)f' + \sqrt{Pr}\frac{1}{2}(\gamma - 1)M_\infty^2(f' - f'^2). \tag{2.30}$$

The expressions above now give both the velocity and temperature distributions over the laminar compressible boundary layer. For an adiabatic wall the wall temperature, Θ_w, can be calculated from eq. (2.30) as,

$$\Theta_w = 1 + r\frac{\gamma - 1}{2}M_\infty^2. \tag{2.31}$$

The factor r is denoted the *recovery* factor, which for a laminar boundary layer is $r = \sqrt{Pr}$. This factor defines how close the wall temperature is to the stagnation temperature.

2.2.4. *The shape factor in compressible flow*

Using the obtained velocity and temperature profiles, the shape factor can be calculated based on the displacement and momentum loss thicknesses defined in eq. (2.16), and eq. (2.17) respectively. Assuming that the perfect gas law gives the density distribution in the boundary layer, the expression

$$H_c = \frac{1.721\Theta_w + 0.664\frac{\gamma - 1}{2}M_\infty^2}{2f''(0)} \tag{2.32}$$

shows the shape factor variation with M_∞. This variation is shown in figure 2.1. Also shown in the figure is the shape factor (H_i) calculated assuming $\rho = \rho_\infty$, and using the velocity distribution obtained from the Howarth-Dorodnitzyn transformed equations. It is observed that the shape factor increases quite rapidly with M_∞ if eq. (2.32) is used (from 2.59 at $M_\infty = 0$ to 3.23 at $M_\infty = 1.0$).

The individual thicknesses can also be calculated, both non-dimensionally, figure 2.2(a), and dimensionally, assuming a stagnation temperature of 30°C and a characteristic distance of $x = 1$ m, figure 2.2(b).
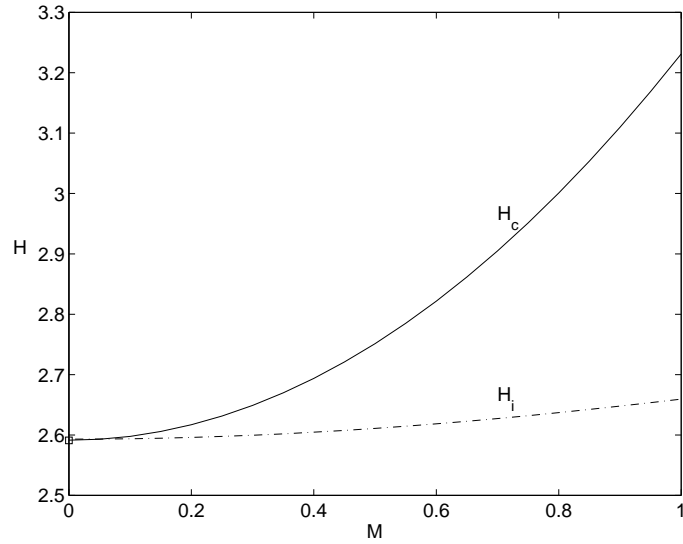
FIGURE 2.1. The shape factor. The dashed line, H_i, is calculated with the incompressible assumption and the full line, H_c, the compressible. The square mark shows the incompressible limit of 2.59.
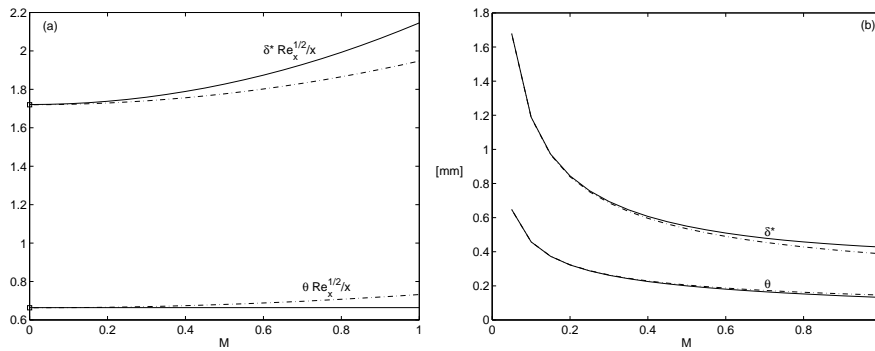

FIGURE 2.2. (a): The displacement thickness and the momentum loss thickness scaled with the Reynolds number. The dashed lines is calculated with the incompressible assumption and the full lines the compressible. (b): The thicknesses assuming $x = 1$ m and $T_0 = 30°$C.

2.3. Turbulent boundary layers

2.3.1. *Averaging in compressible turbulence*

For incompressible flows the equations of motion are Reynolds averaged, *i.e.* the variables are divided into two parts, one mean part,

$$\overline{u} \equiv \int_{t}^{t+\tau} u(t)dt \tag{2.33}$$

and one fluctuating part, u'':

$$u = \overline{u} + u'', \tag{2.34}$$

so that $\overline{u''} = 0$. Here the double prime indicates a fluctuating variable, not a derivative.

For compressible flows the equations of motion become simpler if Favre averaging, mass averaging, is used instead. For Favre averaging, the mass averaged velocity is defined as:

$$\widetilde{u} \equiv \frac{\overline{\rho u}}{\overline{\rho}} \tag{2.35}$$

with the fluctuating part defined as $u' \equiv u - \widetilde{u}$. The tilde denotes the mass weighted average, and the prime a fluctuation from the mass averaged mean. Favre averaged variables are different from Reynolds averaged variables since a time average of the fluctuating part of a variable is in general not zero. This makes statistical results difficult to interpret, though simpler equations are sometimes more preferable. As an illustrative example, the Reynolds averaged form of the continuity equation is:

$$\frac{\partial \overline{\rho}}{\partial t} + \frac{\partial}{\partial x_j} \left(\overline{\rho} \, \overline{u_j} + \overline{\rho' u_j''} \right) = 0, \tag{2.36}$$

and the Favre averaged form is

$$\frac{\partial \overline{\rho}}{\partial t} + \frac{\partial \overline{\rho} \, \widetilde{u}_j}{\partial x_j} = 0. \tag{2.37}$$

Here $\widetilde{u}_j$ is the mean velocity of mass transport, which is not true for $\overline{u_j}$. The simplicity of eq. (2.37) as compared to eq. (2.36) is evident.

2.3.2. *Turbulent boundary layer equations*

The boundary layer equations for a compressible turbulent boundary layer in a steady, two dimensional, adiabatic flow, written in Favre averaged form, are:

$$\frac{\partial \overline{\rho} \, \widetilde{u}}{\partial x} + \frac{\partial \overline{\rho} \, \widetilde{v}}{\partial y} = 0 \tag{2.38}$$

$$\overline{\rho}\widetilde{u}\frac{\partial \widetilde{u}}{\partial x} + \overline{\rho}\widetilde{v}\frac{\partial \widetilde{u}}{\partial y} = -\frac{d\overline{p}}{dx} + \frac{\partial}{\partial y} \left(-\overline{\rho}\widetilde{u'v'} + \overline{\mu}\frac{\partial \widetilde{u}}{\partial y} \right) \tag{2.39}$$

$$\overline{\rho}\widetilde{u}\frac{\partial \widetilde{h_0}}{\partial x} + \overline{\rho}\widetilde{v}\frac{\partial \widetilde{h_0}}{\partial y} = \frac{\partial}{\partial y}\left(-\overline{\rho h_0' v'} + \overline{\mu}\widetilde{u}\frac{\partial \widetilde{u}}{\partial y} + \overline{k}\frac{\partial \widetilde{T}}{\partial y}\right) \quad (2.40)$$

where $h_0 = h + \frac{1}{2}(u^2 + v^2 + w^2)$. If the boundary layer approximated continuity equation is written in Reynolds averaged form,

$$\frac{\partial}{\partial x}\left(\overline{\rho}\,\overline{u}\right) + \frac{\partial}{\partial y}\left(\overline{\rho}\,\overline{v}\right) + \frac{\partial}{\partial y}\left(\overline{\rho'' v''}\right) = 0, \quad (2.41)$$

where the third term, $\frac{\partial}{\partial y}\left(\overline{\rho'' v''}\right)$, acts as a source/sink to the mean flow. The boundary layer approximated x-momentum equation in Reynolds averaged form can be written as:

$$\frac{\partial}{\partial x}\left(\overline{\rho}\,\overline{u}^2\right) + \frac{\partial}{\partial y}\left(\overline{\rho}\,\overline{u}\,\overline{v}\right) = -\frac{d\overline{p}}{dx} + \frac{\partial}{\partial y}\left(\mu\frac{\partial \overline{u}}{\partial y} - \overline{\rho}\,\overline{u'' v''} - \overline{u}\,\overline{\rho'' v''}\right). \quad (2.42)$$

In eq. (2.42), the traditional Reynolds stress can be found, together with another stress term $-\overline{u}\,\overline{\rho'' v''}$ that enhances the incompressible Reynolds shear stress. The Reynolds stress $-\overline{\rho}\,\overline{u'' v''}$, is usually interpreted as the mean rate of transfer of turbulent x-momentum across the plane normal to the y-direction. In a similar way, the term $-\overline{u}\,\overline{\rho'' v''}$ can be interpreted as the mean rate of transfer of turbulent mass flux across the same plane. Finally the boundary layer approximated energy equation in Reynolds averaging has the form:

$$(\overline{\rho}\,\overline{u} + \overline{\rho'' u''})\frac{\partial \overline{h_0}}{\partial x} + (\overline{\rho}\,\overline{v} + \overline{\rho'' v''})\frac{\partial \overline{h_0}}{\partial y} =$$

$$= \frac{\partial}{\partial y}\left[-\overline{\rho v'' h_0''} + \mu\left(1 - \frac{1}{Pr}\right)\frac{\partial}{\partial y}\left(\frac{\overline{u}^2}{2}\right) + \frac{k}{c_p}\frac{\partial \overline{h_0}}{\partial y}\right], \quad (2.43)$$

with $\overline{h_0} = \overline{h} + \frac{1}{2}\overline{u}^2$ and $h_0'' = h'' + \overline{u}u''$ and higher order terms neglected. No additional terms are found, but as seen the convective terms are altered.

Finally the so called Strong Reynolds Analogy (SRA), which is assumed to be valid for adiabatic flows, gives the relation between velocity and temperature fluctuations. A possible mechanism for producing the temperature fluctuations is the convection of the mean temperature field by the velocity fluctuations. In this case it is assumed that u'' and T'' are perfectlty anticorrelated such that

$$R_{uT} = \frac{\overline{u'' T''}}{\sqrt{\overline{u''^2}}\sqrt{\overline{T''^2}}} = -1 \quad (2.44)$$

The temperature-velocity correlation has been measured in experiments by Kistler (1959), who found the correlation to be -0.7. If we assume that the above relation is valid then it is possible to obtain a relation between the velocity and temperature fluctuations

$$\frac{\sqrt{\overline{T''^2}}}{\overline{T}} = (\gamma - 1)M^2\frac{\sqrt{\overline{u''^2}}}{\overline{u}} \quad (2.45)$$

By DNS of turbulent channel flow Huang *et al.* (1995) found that the classical form SRA is not valid for non-adiabatic flows. This is due to the fact that SRA comes from the assumption of the small fluctuations in total temperature, which is not true for the non-adiabatic case.

2.3.3. *Morkovin's hypothesis*

In 1962 Morkovin stated, after analyzing the supersonic boundary layer data available at that time, that for moderate Mach numbers, "The essential dynamics of these shear flows will follow the incompressible pattern". Bradshaw reformulated this hypothesis in 1974 by saying that "high speed boundary layers can be computed using the same models as at low speeds by assuming the density fluctuations are weak". The essentials from Morkovins hypothesis can be concluded to, "apart from changing the local fluid properties the dynamic effects could well be small".

2.3.4. *The temperature field*

With Morkovins hypothesis in mind, what is different comparing the compressible turbulent boundary layer and the incompressible boundary layer? As stated in the hypothesis, the main effect is that the local fluid properties changes due to changes of the temperature across the boundary layer. If ideal gas flow with constant specific heat capacity, c_p, is assumed together with a constant pressure across the boundary layer, the density distribution can be found from the temperature distribution in the boundary layer, using the perfect gas law.

The temperature within a zero-pressure gradient boundary layer is usually assumed to follow the so called Walz' distribution. If one assumes that the temperature is a function of the velocity and also that the turbulent Prandtl number is close to one, one can approximately write (Smits & Dussauge (1996)),

$$\frac{T}{T_\infty} = \frac{T_w}{T_\infty} + \frac{T_r - T_w}{T_\infty}\left(\frac{u}{U_\infty}\right) - r\frac{\gamma - 1}{2}M_\infty^2\left(\frac{u}{U_\infty}\right)^2. \qquad (2.46)$$

where T_w is the actual wall temperature and T_r is the recovery temperature (*i.e.* the wall temperature for an adiabatic wall). r is the recovery factor, the ratio of the increase in temperature at the wall and the temperature increase obtained for an isentropic velocity decrease to zero velocity ($U_\infty^2/2c_p$),

$$r = \frac{T_r - T_\infty}{T_{0\infty} - T_\infty}. \qquad (2.47)$$

The recovery factor for a turbulent boundary layer on an adiabatic flat plate is assumed to be $Pr^{\frac{1}{3}}$, Smits & Dussauge (1996). Walz' relation eq. (2.46) is used extensively and is considered to describe the temperature distribution in the boundary layer satisfactory.

2.3.5. *Turbulent boundary layer scaling*

The turbulent boundary layer has been found to be self similar in an inner and outer region respectively where the dynamics is governed by different length scales. In the inner region the length scale is the so called viscous length scale, defined by

$$\ell_* = \frac{\nu_w}{u_\tau}, \tag{2.48}$$

where the index w denotes the value evaluated at the wall. u_τ is the friction velocity defined as

$$u_\tau = \sqrt{\frac{\tau_w}{\rho_w}}. \tag{2.49}$$

and τ_w is the skin friction,

$$\tau_w = \mu_w (\frac{\partial U}{\partial y})_w, \tag{2.50}$$

The skin friction can be expressed dimensionless as the skin friction coefficient,

$$c_f = \frac{\tau_w}{\frac{1}{2}\rho_w U_\infty^2}. \tag{2.51}$$

The above viscous units are used to non-dimensionalise the physical quantities into a measure also called *plus units*,

$$u^+ = \frac{U}{u_\tau}, \tag{2.52}$$

$$y^+ = \frac{y}{\ell_*}. \tag{2.53}$$

In these plus units different sub-regions can be identified. Close to the wall there is the *linear region* where $u^+ = y^+$, where the viscous forces are dominant. In the *buffer region*, approximately $5 \leq y^+ \leq 30$, there is a smooth change from the linear region to the *logarithmic region* approximately from $y^+ \approx 30$ to $y/\delta = 0.15$. The logarithmic region is covered by both inner and outer scaling and is also called the *overlap region*. The logarithmic region can be expressed as

$$u^+ = \frac{1}{\kappa} \ln y^+ + C, \tag{2.54}$$

where κ is the von Karman constant and C the intercept with the u^+ axis. Both κ and C are empirical constants and the values of the constants are still debated with values of $0.38 \leq \kappa \leq 0.41$ and $4.0 \leq C \leq 5.2$ (see for instance Österlund (1999)).

In the outer region, the so called *wake region*, viscosity is less important, but the presence of the wall still has an influence through the magnitude of the shear stress. The relevant outer length scale is

$$\Delta = \frac{\delta^* U_\infty}{u_\tau}, \tag{2.55}$$

and the variable for the wall normal direction is

14

$$\eta = \frac{y}{\Delta}. \tag{2.56}$$

In the outer region the velocity is made non-dimensional as a defect and the relevant velocity scale is still the friction velocity giving

$$U_\Delta = \frac{U_\infty - U}{u_\tau}. \tag{2.57}$$

For the outer layer, the expression equivivalent to the log law is:

$$U_\Delta = -\frac{1}{\kappa} \ln \eta + B \tag{2.58}$$

where B can be calculated as

$$B = \frac{U_\infty}{u_\tau} - \frac{1}{\kappa} \ln \frac{\delta^\star U_\infty}{\nu} - C \tag{2.59}$$

and becomes close to 3.6 for κ=0.38.

For compressible flow the so called Van Driest transformation has been introduced and has been shown to allow compressible boundary layer data to be compared to incompressible data. The transformation is

$$U_c = \int_0^u \sqrt{\frac{\rho}{\rho_w}} du. \tag{2.60}$$

Since the pressure is constant through the boundary layer this can be rewritten using the perfect gas law such that

$$U_c = \int_0^u \sqrt{\frac{T_w}{T(u)}} du. \tag{2.61}$$

Inserting Walz' relation eq. (2.46), in the above expression,

$$U_c = \int_0^u \sqrt{\frac{1}{1 - a_1 u^2 + a_2 u}} du, \tag{2.62}$$

with

$$a_1 = \frac{r}{2c_p T_w}, \tag{2.63}$$

and

$$a_2 = \frac{T_r/T_w - 1}{U_\infty}, \tag{2.64}$$

then the final expression for the transformed velocity is:

$$U_c = \frac{1}{\sqrt{a_1}} \left[\arcsin \frac{2a_1 u - a_2}{\sqrt{4a_1 + a_2^2}} + \arcsin \frac{a_2}{\sqrt{4a_1 + a_2^2}} \right]. \tag{2.65}$$

For an adiabatic wall a_2 is equal to zero and the second term vanishes and the expression reduces to

$$U_c = \frac{1}{\sqrt{a_1}} \left[\arcsin \sqrt{a_1} u \right]. \tag{2.66}$$

For Mach numbers below one the argument $\sqrt{a_1}u$ is in general small so that the RHS can be series expanded such that

$$U_c = u \left[1 + \frac{a_1 u^2}{6} \right]. \tag{2.67}$$

2.4. Shock wave/boundary layer interaction

The pressure rise across a shock wave results in an increase of the boundary layer thickness. Due to the thickening of the boundary layer, compression waves forms upstream the shock wave. When the shock wave becomes strong enough and the thickening of the boundary layer large enough the compression waves coalesce into an oblique shock wave upstream the other shock wave and a lambda shock is formed.

A sketch of a lambda shock wave/boundary layer interaction can be found in figure 2.3. The first oblique shock, usually denoted the C_1 shock, is the
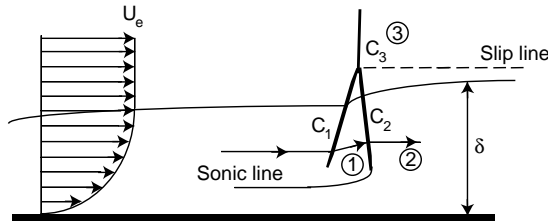

FIGURE 2.3. A lambda shock system.

oblique shock formed by compression waves and is a weak solution to oblique shock theory. Where the C_1 shock meet the quasi-normal shock located in the far outer field, denoted as the C_3 shock, two states with different pressures and velocity inclinations, ① and ③, exist. At the intersection of these shocks the states are not compatible, therefore a third shock is created, which is named the C_2 shock.

The factors that determines if the adverse pressure gradient downstream the C_2 shock is strong enough to cause boundary layer separation, are the Mach number upstream the shock and the shape factor calculated with the assumption of incompressibility, Delery & Marvin (1986). The shape factor has a weak influence on the onset of separation, leaving the Mach number ahead of the shock as the principal parameter. For a shape factor of 1.50 the Mach number should be higher than 1.25 to cause separation but if the shape factor is reduced to 1.20 the Mach number has to be increased to 1.32 for separation to occur. The results were found by investigations in several different experimental setups, such as a mounted wing profile in the test section and a bump on the wall. For a wall with curvurature of $\delta/R < 2$ %, where δ is the boundary layer thickness upstream the shock and R the radius of the curvature. The effect of

the curvature is small and similar to that of increasing the shape factor, Inger & Sobieczky (1978) and Nandanan *et al.* (1980).

Raghunathan & McAdam (1983) investigated the influence of free-stream turbulence on the shock wave/boundary layer interaction on a bump model. They found that if the free-stream turbulence (FST) level was increased from 0.3% to 6% the shock location was shifted 20% further downstream relative to the starting point of the bump. This shift in shock location could not be explained solely by the thickening of the boundary layer due to the increase in FST but no other explanation was proposed.

The transonic flow over a thick circular arc airfoil was experimentally investigated by McDewitt *et al.* (1975). They found that up to a critical Mach number the flow was steady with boundary layer separation near the trailing edge ($M_e = 0.76$). Increasing the Mach number slightly the flow became unsteady with the separation oscillating between the trailing edge and the base of the shock with a frequency of about 190 Hz. A further increase of the Mach number (to $M_e = 0.78$) resulted again in steady flow but with the separation located at the base of the shock foot.

Shock wave oscillations have been categorised for the transonic flow over an airfoil and are known as Tijdeman (1977) type A, B and C.

Type A is a small amplitude almost sinusoidal motion and can be explained in the following way. Consider a transonic flow over a wing profile with shock waves on both sides attributed to an asymmetric disturbance causing a higher Mach number on the upper side. Let the Mach number on the upper side be strong enough to cause shock wave induced separation and hence the wake at the tail of the wing profile will be deflected upwards. The change in the flow geometry will cause the shock wave on the lower side to move towards the tail. At the same time the shock wave on the upper surface will move upstream into lower velocities and thus weaken and the boundary layer will reattach. This will cause shock wave induced separation on the lower side of the wing profile with deflection of the wake downwards, and the cycle will repeat itself, Lee (1990) and Raghunathan *et al.* (1998).

The type B motion is similar to type A, but with an amplitude high enough to cause the backwards moving shock wave to disappear at its most upstream position. Type C has an even larger shock motion amplitude and the shock propagates upstream into the free stream as a weak and free shock wave during part of the cycle, see Tijdeman & Seebass (1980) for further details.

For a bump on the wall the shock wave in transonic flow can exhibit an oscillatory motion. The motion can be explained with similar arguments as for Tijdemans type A motion. When the shock wave on the bump becomes strong enough to cause a considerable boundary layer growth, the flow geometry changes and the shock wave moves upstream. As the shock wave moves upstream it becomes weaker, the boundary layer growth declines, and the shock wave moves downstream. It has been shown in supersonic flow when the shock wave is strong enough to cause shock induced separation, the shock wave shows

17

something similar to a high frequency motion superimposed on a low frequency oscillation, Dolling & Murphy (1983). The low frequency oscillation has been found to correlate with the low frequency pressure fluctuations of the separation bubble, Erengil & Dolling (1991).

CHAPTER 3

Experimental facility and setup

3.1. Experimental facility

The wind tunnel used in the present study is one of several exchangeable test rigs in a larger experimental facility located at the Department of energy technology, KTH. The flow facility consists of a screw compressor which is located outdoors, a cooler, the experimental rig and an exhaust fan. A drawing of the system is shown in figure 3.1. The outdoor screw compressor (1.3 MW) delivers 4.7 kg/s air at a maximum of 4 bars absolute pressure and at a temperature of 180°C. The compressed air is cooled in a heat exchanger from 180°C to a value at will (minimum 30°C) and conducted through a 40 cm diameter pipe system to the test rig. The air to the compressor is taken from the outside air which means that the humidity of the air provided to the tunnel is the same as for the outside air since no drying is provided. This may lead to fog in the tunnel when the flow accelerates and the temperature decreases. After passing the test section the air is released to the outdoor via the exhaust fan.
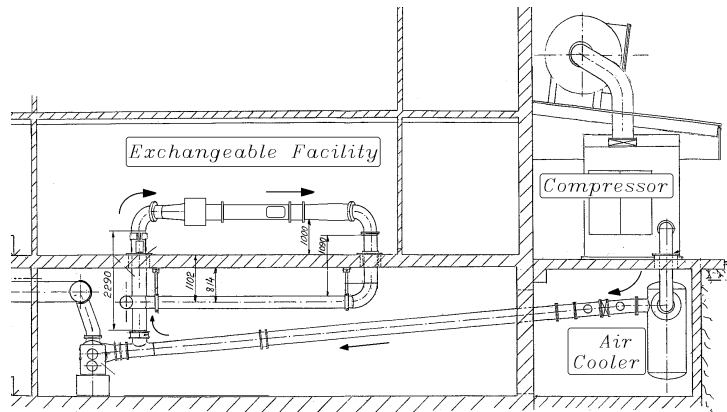

FIGURE 3.1. The transonic wind-tunnel with, compressor, cooler and pipe system.

The mass-flow rate, inlet and outlet pressures in the test section are regulated through the inlet, outlet and bypass valves and the speed of the exhaust fan, figure 3.2.
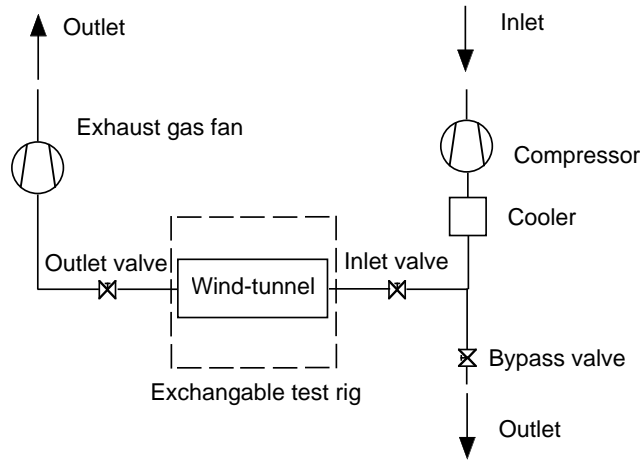
FIGURE 3.2. A flow chart of the experimental facility.

3.2. Wind-tunnel

The air is coming from the compressor through a guide-vane equipped corner to the inlet part of the wind-tunnel and a honeycomb guides the flow into the 250×250 mm^2 stagnation chamber. This chamber is equipped with screens and located 1.5 m upstream of the test section. A first contraction in the horizontal plane conducts the flow into the vertical contraction located 30 cm upstream of the test section. After the contractions the tunnel area is slightly increased to compensate for boundary layer growth. The test section is 100 mm wide and 120 mm high with an exchangeable test 'floor' where a flat plate or a bump model can be mounted. For a schematic view of the wind tunnel see figure 3.3.
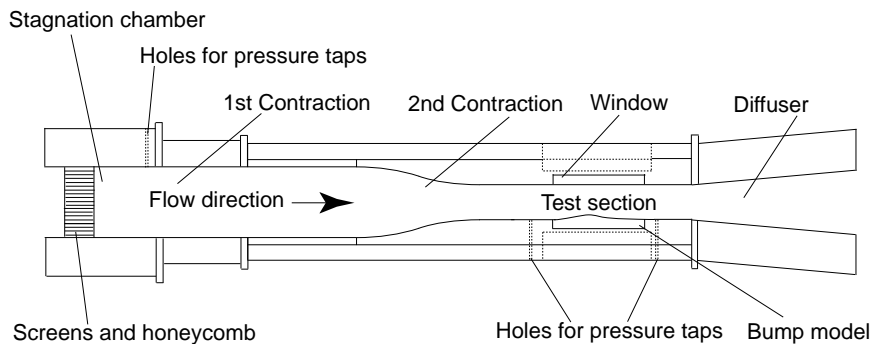

FIGURE 3.3. A side-view of the transonic wind-tunnel.

There are two different bump models available, a 2D bump and a 3D bump. In this investigation the flat plate and the 2D bump has been used. The maximum height of the bump is 10.5 mm. The test section with the 2D bump inside is shown in figure 3.4.
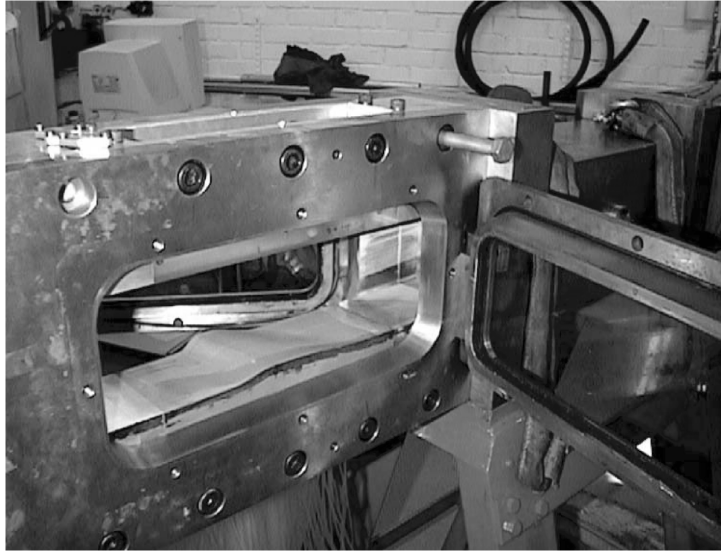

FIGURE 3.4. The bump-model in the test section.

The test section ceiling and side windows are exchangeable and optical glass or Plexiglas windows can be inserted. This allows optical measuring methods such as LDV, PIV and schlieren techniques. In the Plexiglas windows, holes for pressure taps are located. Static pressure holes are also located in the floor at the inlet and outlet of the test section.

The stagnation temperature is measured with a copper-constantan thermocouple. The thermocouple is mounted in a pipe which is directed towards the oncoming flow in the stagnation chamber.

3.3. Digital Particle Image Velocimetry

The DPIV technique measures the fluid velocity by determining the displacement in a given time interval of small tracer particles suspended in the fluid. A thin high intensity laser sheet illuminates the particles and a CCD camera placed normal to the laser sheet records the particle distribution in the plane and stores the image digitally. The flow field is exposed twice with a short time interval and the images are either stored on separate frames or on the same frame. The image is divided into a number of small areas, so called interrogation areas, with the assumption that within each area the velocity should

be constant. The mean particle displacement between the exposures is determined through a two dimensional cross- or auto-correlation process dependent on the type of storage chosen. This gives the velocity vector variation over the illuminated plane, both with respect to its direction and absolute magnitude.
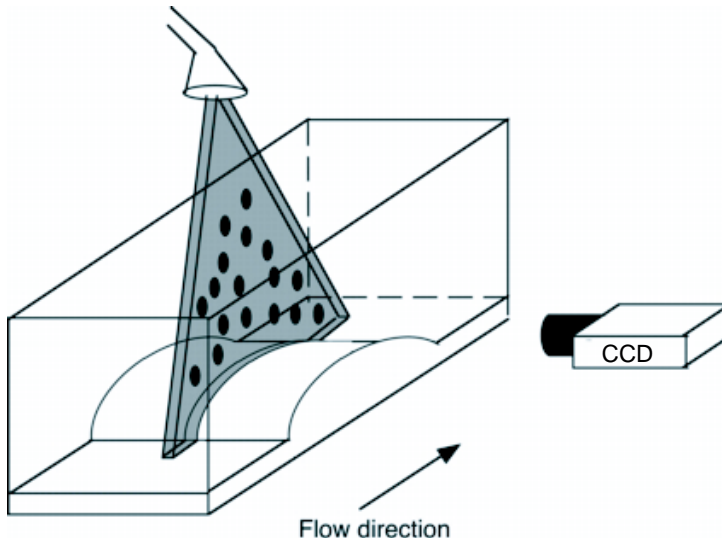

FIGURE 3.5. A schematic of the PIV setup.

The correlation of the light intensity distribution $I(\vec{x})$ in each interrogation area is given by:

$$R_c(\vec{s}) = \int_{ia} I_1(\vec{x}) I_2(\vec{x} + \vec{s}) d\vec{x},$$

where $\vec{s}$ is a two dimensional displacement vector. $I_i(\vec{x})$ is the light intensity distribution in image i, which for an auto-correlation method gives $I_1(\vec{x}) = I_2(\vec{x})$. The highest R_c for $|\vec{s}| \neq 0$ gives the most likely displacement in the interrogation area. With auto-correlation it is not possible to determine the flow direction since it is not possible to distinguish which particles come from the the first exposure and which come from the second.

To decrease the time to carry out the correlation calculations, the images are Fast Fourier Transformed (FFT). The Fourier transform of an interrogation area from the first image is multiplied with the complex conjugate of the corresponding transformed interrogation area from the second image and then inversely transformed to obtain the correlation function R_c. The position of the maximum cross-correlation peak, or the second highest auto-correlation peak corresponds to the most probable particle displacement in the interrogation areas between the two exposures.
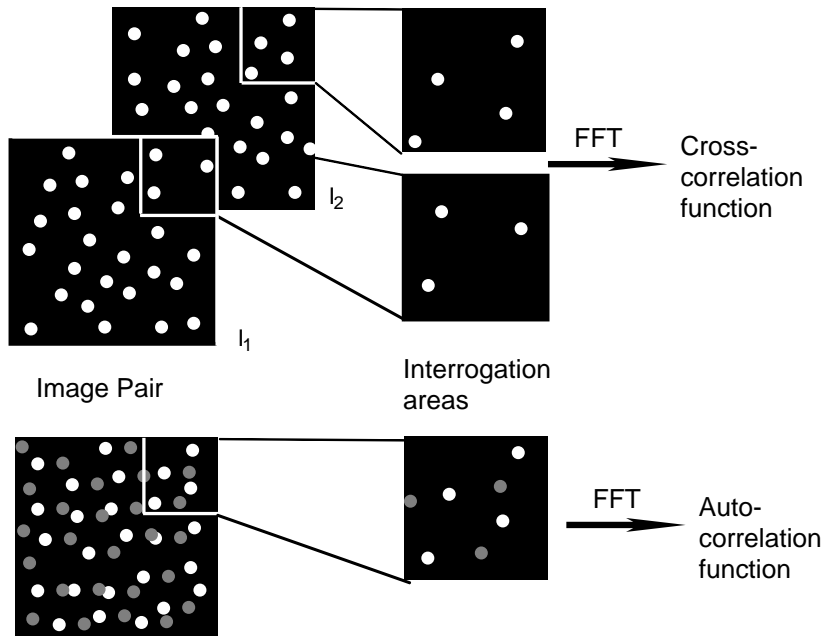
FIGURE 3.6. A schematic of the PIV analysis. The white dots are the seeding particles. The grey dots are the particles for the second exposure (in auto-correlation mode).

3.3.1. *Particle considerations*

3.3.1.1. *Light scattering from small particles*

The intensity of the scattered light from small particles is two to three orders of magnitude lower normal to the laser sheet than to the incident light, which is the reason why high intensity lasers are needed as light sources. The light intensity in the images decreases as $I \sim l^{-2}$, where l is the distance between the light scattering particle and the camera.

For spherical particles with a particle diameter of the order of the wavelength of the illuminating light, Mie scattering theory has to be applied to estimate the scattered light in different directions. The most important factors affecting the scattering power are the particle diameter and relative refractive index and the scattering power increases both with the particle size and the relative refractive index, see Adrian & Yao (1985).

3.3.1.2. *Dynamical behaviour of small particles*

The dynamics of particles in a fluid is given by Newton's second law which states that the mass of the particle times its acceleration is equal to the forces acting on the particle. The important forces are here the fluid dynamic forces which are due to a velocity difference between the particle and the fluid, whereas it

is assumed that external forces, such as gravitational, centrifugal and electro-static, can be neglected. The equation governing the dynamics of particles is usually denoted the BBO-equation (Basset-Boussinesq-Oseen) and is for spherical particles given by (see for instance Hinze (1975))

$$
d_p^3 \rho_p \frac{\pi}{6} \frac{dU_p}{dt} = -3\pi\mu d_p V + \frac{\pi}{6} d_p^3 \rho_f \frac{dU_f}{dt} - \frac{\pi}{12} d_p^3 \rho_f \frac{dV}{dt}
$$

$$
-\frac{3}{2} d_p^2 \sqrt{\pi\mu\rho_f} \int_{t_0}^{t} \frac{dV}{d\chi} \frac{d\chi}{\sqrt{t-\chi}}, \tag{3.1}
$$

where subscripts p and f, refer to the particle and fluid respectively, V is the instantaneous velocity of the particle relative to the fluid, $V = U_p - U_f$. The first term on the right hand side is the viscous drag given by Stokes law, which then implies that the particle Reynolds number ($V d_p/\nu$) is smaller than one. The force on the particle due to the pressure gradient in the vicinity of the particle produced by the particle's acceleration is described by the second term. The third term is a measure of the force required to accelerate the fluid around the particle in a time dependent flow field ("added mass" term). The last term is a so called history term associated with unsteady motion.

For practical applications with a large ratio between the particle and fluid densities, only the first term on the RHS in eq. (3.1) is important and the equation of motion can be written as

$$
\frac{dU_p}{dt} = -\frac{18\mu}{d_p^2 \rho_p} V. \tag{3.2}
$$

Assuming a step change in velocity, eq. (3.2) gives the relaxation time for a particle encountering the change in velocity as:

$$
\tau_p = \frac{1}{18} \frac{\rho_p}{\rho_f} \frac{d_p^2}{\nu}. \tag{3.3}
$$

For turbulence measurements the particle size should not exceed the smallest turbulent eddies and the density of the particle should be as close as possible to the density of the fluid in order to follow the turbulent motion. For particles with a density higher than the fluid the size of the particles has to be quantified with respect to the highest turbulence frequency of interest. This frequency can be estimated with the Kolmogorov time scale, $\tau_k = \sqrt{\nu/\epsilon}$, where ϵ is the local turbulence dissipation.

Particles commonly used in measurements of gas flows are generated from polyethylenglycol or silicon oil with a diameter of about 1 μm and a density of about 700 – 900 times that of air. These particles have a spherical shape and are easy to produce. The maximum frequency that can be resolved with these kind of particles is about 10 kHz, Melling (1997). Titaniumdioxide particles with a density of 3000 times that of air are also used. These particles with a diameter of 1 μm have a frequency response of 1 kHz, but if the diameter

is decreased to 0.5 μm the frequency response increases to 10 kHz. Other commonly used particles are made of Al_2O_3, glycerine and MgO.

In the present study the most critical point of particle dynamics is the passage of particles through the shock. Assuming particles with a density of $1000\,\text{kg/m}^3$ in a flow across a shock wave with the Mach number 1.30 upstream the shock and 0.79 downstream the shock, the relaxation length for a particle with a diameter of 1 μm is about 12 mm. The size of the particles should be less than 0.3 μm to have a relaxation length shorter than 1 mm, for further details see Melling (1997). The shock strength is however not influencing the relaxation length, Ross $et\ al.$ (1994).

3.3.2. *Validation*

Data validation for PIV mainly means the detection and removal of spurious velocity vectors. These vectors are considered unrealistic in relation to neighbouring velocity vectors and are often caused by insufficient numbers of particle pairs in the interrogation areas due to low particle density, high number of particle losses between exposures or low signal to noise ratio in the image. The particles that most likely are lost are those moving out of the plane and the particles with the highest velocity. This means that the measurement is biased towards a lower velocity than the real one. The particles from the first exposure that corresponds with particles lost in the second, can however be correlated with other particles in the second exposure, for instance particles entering an interrogation area. These correlations are denoted random correlations and decrease the signal to noise ratio.

To get a high signal to noise ratio in the correlogram a relative high number of particles in each interrogation area is needed. The amount of particles that are required in each interrogation area to ensure a 95 % valid detection rate of the correlation peak, has been investigated by different authors with the use of Monte Carlo simulations. The authors found that, for cross-correlation, 5–7 particles in each interrogation area are needed (Keane & Adrian (1992), Dantec (1998)) and, for auto-correlation, 10–20 particles/interrogation area (Adrian (1991)). With auto-correlation, a higher amount of particles are needed in each interrogation area since the amount of random correlations are higher.

In order to minimise loss of pairs and to sort out true correlations from random correlations, the particles are not allowed to have travelled further than 25 % of the interrogation area sidelength. An implementation of the criteria is to set the time between the exposures. The maximum time between two exposures can be determined as

$$t \leq \frac{1}{4}\frac{\ell_{ia}L_{im}}{N_{px}U_{max}}, \tag{3.4}$$

where ℓ_{ia} is the interrogation area sidelength of the image in pixels, L_{im} the physical image sidelength, N_{px} the sidelength of the image in pixels, and U_{max} the maximum velocity in the interrogation area.

Furthermore the detectability of the correlation peak, the Peak Value Ratio (PVR), the ratio of the highest cross-correlation peak to the second highest (second highest auto-correlation peak to the third highest), should not be smaller than 1.20. Together with the seeding requirement, this should result in 95 % validated correlations according to Keane & Adrian (1992). Angele (2003) investigated the influence of the PVR when increasing the limiter from 1.20 to 1.50 by comparing turbulent boundary layer data measured with PIV and hot-wire anemometry. The influence of the validation in the mean velocity was none and in the velocity *rms* negligible. This leaves the conclusion that a PVR of 1.20 is sufficient and an increase does not necessarily mean that random correlations are removed but true correlations can be removed as well.

3.3.3. *The PIV system*

The measurements were performed with a system consisting of a Quanta Ray GCR-series Nd:YAG laser, a Dantec light guide arm with optical head and laser sheet forming optics, a Kodak ES 1.0 CCD camera and a Dantec PIV 2000 software. The Nd:YAG laser has two laser cavities that can be fired individually at a maximum repetition rate of 15 Hz and the peak energy in the 4 ns long laser pulse is 0.4 J. The light sheet optics forms a 1 mm thick laser sheet with a Gaussian intensity distribution at the beam waist.

The camera has 1018×1008 pixels and a dynamic range of 256 grey-scale levels. The first image is stored in buffer cells in the CCD-chip before the second image is captured. The transfer between sensing element and buffer is instant and the time between two successive images can be brought down to 1 μs. The transfer of the two images to the computer is however slow and limits the data rate.

The PIV system operates both in cross-correlation and auto-correlation modes, however, to achieve separations between exposures shorter than 1 μs the camera has to be run in auto-correlation mode and the timing between laser pulses has to be controlled by an external pulse delay generator (Stanford Research DG535).

3.4. The oil-drop method

An important variable in boundary layer research is the wall-shear stress. In the present project the oil-drop method was used as an independent measurement of the skin friction on the flat plate and the method is briefly described here.

The basis of the oil-drop method is to measure the change in thickness of a drop of oil on the wall while the drop is deformed by the skin-friction of the boundary layer. The variation of the thickness of the oil drop is measured using an interference method. The film thickness can be visualised by Fizeau fringes of alternately high and low light intensity which originate from the interference of light reflected from the top and bottom of the oil-film. The height of the kth black fringe is

$$h_k = h_0 + k\Delta h \quad k = 0, 1, 2 \dots \tag{3.5}$$

with

$$\Delta h = \frac{\lambda}{2\sqrt{n^2 - \sin^2 \alpha}} \qquad (3.6)$$

where h_0 is the height of the zeroth black fringe, Δh the difference in height from two neighbouring fringes, n the refractive index of the oil, α the viewing angle and λ the wavelength of the illuminating light. This means that the fringes are contour lines of the height of the oil film.
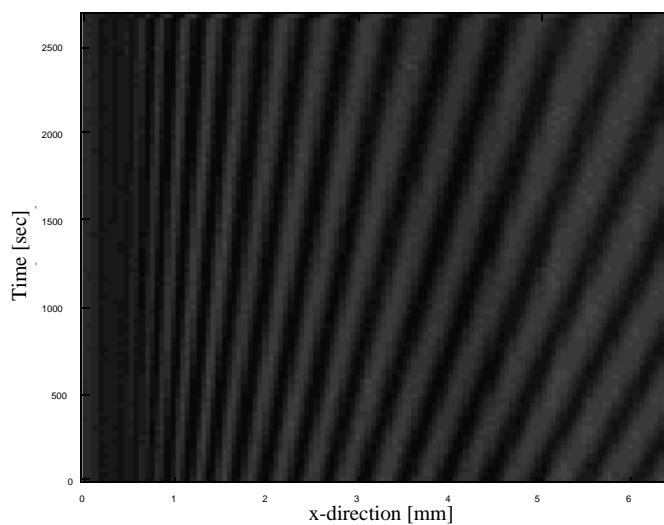

FIGURE 3.7. $x - t$ diagram for the oil-drop method. Picture from Medici (1999), with permission.

The motion of the fringes along a straight line is recorded in an $x - t$ diagram, figure 3.7. The temporal development of the height of a thin 2D oil film affected by a surface shear that only varies in the streamwise direction of the flow, is described by

$$\frac{\partial h}{\partial t} = -\frac{1}{2\mu}\frac{\partial(\tau h^2)}{\partial x}, \qquad (3.7)$$

where τ is the shear stress. Assuming constant shear stress ($\overline{\tau}$) in time and space, eq. (3.7) can be reduced to

$$\frac{\partial h_k}{\partial t} + u_k \frac{\partial h_k}{\partial x} = 0, \qquad (3.8)$$

with $u_k = \overline{\tau} h_k / \mu$, where u_k is equivalent to the slopes of the contour lines in the $x - t$ plane. The above eqs. (3.5) – (3.8), together give

$$\overline{\tau} k + \overline{\tau}\frac{h_0}{\Delta h} = \mu u_k \frac{2\sqrt{n^2 - \sin^2 \alpha}}{\lambda}, \qquad (3.9)$$

27

which is an over determined system for a number of u_k measured in an $x - t$ diagram. A simple least square fit gives the unknown quantities $\overline{\tau}$ and $h_0/\Delta h$.

CHAPTER 4

Hot-wire anemometry

Velocity measurements in compressible flows are more complex than in the incompressible case, since in general not only the flow velocity varies, but also the temperature and the density of the gas as well as the viscosity of the gas. Furthermore if a probe (for instance a pitot tube or hot wire) is inserted in the flow not only the gas velocity will be zero at the probe surface, but the gas properties will change from its undisturbed conditions. The fact that 'everything varies' in compressible flow makes the use of intrusive measuring techniques more complicated than for the incompressible case and in order to get accurate absolute measurements a calibration and evaluation technique must be able to take these different variations into account. In this chapter a calibration technique for hot-wire measurements in compressible flows for Mach numbers up to 1 is described and evaluated.

The principle of hot-wire anemometry is based on the fact that the cooling of a heated body immersed in a moving fluid depends on the flow velocity (for the basics of hot-wire anemometry see for instance Bruun (1995)). Although hot-wire anemometry is a well known technique for incompressible flows and in that case can give accurate results both for mean and fluctuating quantities, it has been much less used in compressible flow cases. Still it has a lot of advantages since it gives a continuous signal allowing frequency information as well as a rather small, at least in two directions, measuring volume. For instance Kosinov *et al.* (1990) used hot-wire anemometry to investigate the growth of wave disturbances in a laminar boundary layer at a Mach number of 3. In that study the probe was located at different downstream positions but at a position inside the boundary layer where the mean voltage was constant, thereby ensuring that the position was the same in terms of the velocity. The *rms* of the raw hot-wire signal was then used to evaluate the growth/decay of the waves. With this methodology they avoided the problem to do absolute calibrations of the system.

In the anemometer set up the probe is connected to one arm in a Wheatstone bridge. Because of the small diameter of the wire most of the electrical resistance (typically 1-20 ohms) of the probe and cablage is associated with the wire itself. By providing a voltage difference across the Wheatstone bridge a current flows through the wire and heats it. Typically it is heated to 100-200 degrees above ambient temperature. A servo amplifier keeps the bridge in balance by controlling the voltage across the bridge, giving a varying current

through the wire in such a way that the resistance of the wire, R_{hw}, is kept constant, independent of the cooling imposed by the fluid. This also means that the mean temperature T_{hw} of the wire is constant. This mode of operation is referred to as Constant Temperature Anemometry (CTA).

For CTA-operation the square of the current through the wire is proportional to the electrical power generated and hence this is also the heat transfer to the wire surroundings. To obtain good operating conditions it is necessary that the main part of the heat flux is directly from the wire to the fluid, however a certain amount is fed to the prongs by heat conduction. This is the reason why the length to diameter ratio of the wire should be as high as possible.

The current through the wire is directly proportional to the voltage across the Wheatstone bridge and this voltage (or a voltage proportional to it) is usually provided as the anemometer output. The combination of the sensor's low thermal inertia and the high gain of the servo loop amplifier gives a fast response to fluctuations in the flow. This makes it possible to resolve also very high frequency fluctuations, such as small vortices that are convected by the mean flow. However one problem which need to be addressed when measuring in turbulent flows is the spatial resolution of the probe. Even a 1 mm long wire may be much too long to resolve typical length scales in *e.g.* a turbulent boundary layer at high velocities.

4.1. Heat transfer from a cylinder

The heat transfer from a cylindrical body can be given in terms of the non-dimensional Nusselt number

$$Nu = \frac{hd}{k}$$

where h is the heat transfer from the cylinder to the fluid, d is the cylinder diameter and k the heat conductivity of the fluid. By ignoring the radiative heat ransfer the most general form of the convective heat transfer from an infinite long cylinder to a gas expressed in non-dimensional parameters is

$$Nu = Nu(Re, Pr, Gr, M, Kn, \tau) \tag{4.1}$$

Here $Re(= \rho U d/\mu)$ is the Reynolds number based on the gas density ρ, the flow velocity U, the wire diameter d, and the dynamic viscosity μ. The density and dynamic viscosity is usually evaluated at the mean temperature of the wire and the surrounding gas. The Prandtl number, $Pr = \nu/\alpha$, where α is the thermal diffusivity, is constant for conditions not too far from atmospheric. For instance, the Prandtl number of air varies only 3% when the temperature changes from 0°C to 100°C. The Grashof number describes the influence of free convection, but is of no importance for the high velocity flows considered here.

M is the Mach number, defined as $M = U/\sqrt{\gamma RT}$, where γ is the ratio between the specific heats at constant pressure c_p and volume c_v (also called

the adiabatic exponent), R is the specific gas constant and T the absolute temperature of the gas. For air at moderate temperatures γ is close to 1.40 whereas $R = 287$ J/kg K.

Under most circumstances a gas can be described as a continuum but this is not necessarily a good approximation for high speed gas flows. The Knudsen number Kn gives the relation between a characteristic length, here the wire diameter, and the the mean free path of a gas molecule, such that $Kn = \lambda/d$, where the mean free path, λ, can be expressed as

$$\lambda = \frac{\mu_\infty}{\rho_\infty}\sqrt{\frac{\pi}{2RT_\infty}}.$$

For a gas at standard conditions $\lambda \approx 0.06$ μm, but increases with decreasing pressure. Usually one assumes that if $Kn \leq 0.01$ the fluid can be considered as a continuum and the heat transfer is then independent of the Knudsen number.

Finally τ is the overheat ratio, defined as, $\tau = (T_{hw} - T_0)/T_0$, with T_0 as the stagnation temperature of the flow, and T_{hw} the wire temperature. Since the wire temperature operated by a CTA is constant, the overheat ratio varies with the stagnation temperature only.

4.1.1. *Heat transfer in incompressible flow*

For incompressible flow in air ($M = 0$) at near standard conditions Kn can be viewed as sufficiently small to allow for the continuum hypothesis and the Prandtl number can be viewed as a constant. If the air velocity is larger than typically 0.3 m/s then the Grashof number is small enough so that forced convection will completely dominate the heat transfer to the gas. This means that eq. (4.1) reduces to

$$Nu = Nu(Re, \tau) \tag{4.2}$$

The Nusselt number for the wire is proportional to the power input, *i.e.* it is proportional to the square of the output voltage from the anemometer, E^2. For a given overheat ratio it is possible to express the output voltage in terms of the flow velocity such that

$$E^2 = A + BU^n \tag{4.3}$$

This equation is often referred to as King's law. The dependence of ρ and μ are included in the calibration constants A, B and n in eq. (4.3). King (1914) derived an expression for the heat transfer around an infinitely long cylinder and obtained a value of the exponent n of 0.5, and from calibration data an exponent close to 0.5 is usually found. The constant A can be seen to equal the square of the voltage at zero velocity, however usually A is slightly less than that. This is because free convection becomes important when the flow velocity is low giving a larger heat transfer than would otherwise be the case.

4.1.2. *Heat transfer in compressible flow*

In compressible flow one has to take into account also other variables than the velocity when evaluating the hot-wire output signal. This is not only true for the mean voltage but also for fluctuations of velocity, density and temperature, Kovasznay (1953). This makes the calibration method for compressible flow more complex since also these quantities have to be varied.

However, one can usually assume that Gr and Kn both are small and that the Prandtl number is constant, which makes eq. (4.1) reduce to:

$$Nu = Nu(Re, M, T_0) \tag{4.4}$$

Using King's law, eq. (4.3), as an ansatz also for compressible flow, the following relation is suggested

$$Nu = A'(M, T_0) + B'(M, T_0)Re^n \tag{4.5}$$

The generalization of King's law means that the constants A' and B' are allowed to vary with the Mach number and the stagnation temperature. The variable in the relationship is changed to the Reynolds number, instead of the velocity alone. If the viscosity and wire diameter in the Reynolds number are included in the functions A' and B' in eq. (4.5) it can now be written for a given gas as

$$E^2 = A(M, T_0) + B(M, T_0)(\rho U)^n \tag{4.6}$$

The above expression, eq. (4.6), is now the calibration function for hot-wires in subsonic compressible flow, 'King's law for compressible flow'. If the functions $A(M, T_0)$, $B(M, T_0)$ and the exponent n are found in a calibration process, then the velocity can be calculated, a procedure which will be described in section 4.2.4. For incompressible flow, where the Mach number is zero, and the density and stagnation temperature are constant, eq. (4.6) reduces to the ordinary King's law, eq. (4.3).

Another factor that may influence the heat transfer from a hot wire is the air humidity. Schubauer (1935) studied this influence and found that when the humidity was changed from 25 to 70 percent with a surrounding temperature of $25°C$, a 2 percent change in the Nusselt number was observed. The explanation was given by the high thermal conductivity of water which is believed to raise the thermal conductivity of the air.

4.2. Calibration method

4.2.1. *Calibration set-up*

The calibration was performed in a TSI calibrator unit model 1127, figure 4.1. This unit produces a jet of variable speed and the hot wire is placed in the potential core of the jet. The calibrator unit consists of a 270 mm long stagnation chamber with a diameter of 110 mm, and an exit nozzle. In the stagnation

chamber there are screens at half the chamber length to reduce mean flow variations and decrease turbulent fluctuations in the jet. The nozzle diameter can be changed by replacing the entire nozzle. Four nozzle sections with different diameters are available with diameters of 3, 6, 10 and 14 mm and the smaller the nozzle the higher the maximum outlet velocity. The air to the calibrator was obtained by a 2.2 kW compressor which could deliver a pressure up to 8 bar.

In order to calibrate the hot wire at different densities the outlet pressure has to be varied. This was made possible by letting the jet flow into a Plexiglas container in which the static pressure could be varied by applying suction or blockage at the top of the container, see figure 4.1(b). At first the enclosing caused vibrations of the probe due to vortices appearing between the container wall and the nozzle, but this problem was eliminated by inserting a secondary tube with holes close to the nozzle. The setup is similar to that of Johnston & Fleeter (1997).

To allow the stagnation temperature to be changed, a heater was added between the pressure regulator and the calibrator. The heater consisted of a tube with resistive wire from a hairdryer in the centre of the tube. The wire was heated by applying a current from a power supply. The stagnation temperature could then be adjusted from ambient temperature up to 50°C.

For high Mach numbers the 3 mm diameter nozzle has to be used since the mass flux of the compressor system is limited. Even though the hot wire is positioned close to the nozzle exit in the potential core the finite size of the probe may influence the calibration results. Therefore a "classic calibration" was performed to investigate the effect of changing the nozzle size. By the term "classic calibration" it is meant that the probe was placed in the jet where the stagnation temperature was held constant and the stagnation pressure was changed in order to vary the velocity. This was performed with the nozzle diameters 3 mm and 6 mm. The curves can be found in figure 4.3. The curves differ by 1 % in the velocity or 0.2 % in the voltage showing that the small size of the 3 mm nozzle does not influence the calibration results.

4.2.2. *Hot-wire probe*

For the present measurements home made single hot-wire probes were used, figure 4.4. The hot-wire probe body was a ceramic tube designed for thermoelement use with a diameter of 2.7 mm. The prongs were made of spring steel. According to potential theory the length of the prongs should be at least 6 body diameters, in order for the probe body not to affect the flow. However the prongs are glued to the probe body with a low viscosity resin in a streamlined fashion, thus making the necessary length shorter. The prong length here is 15 mm, or 5.6 diameters. The conical shape of the prong tips were obtained by an etching of the prongs in nitric acid (60 %). The positioning of the prongs in the probe body were done with micro manipulators under a 80× microscope.

1. Heater
2. Stagnation Chamber
3. Probe Holder
4. Filter

(a)

(b)

Suction or blockage

Airtight container
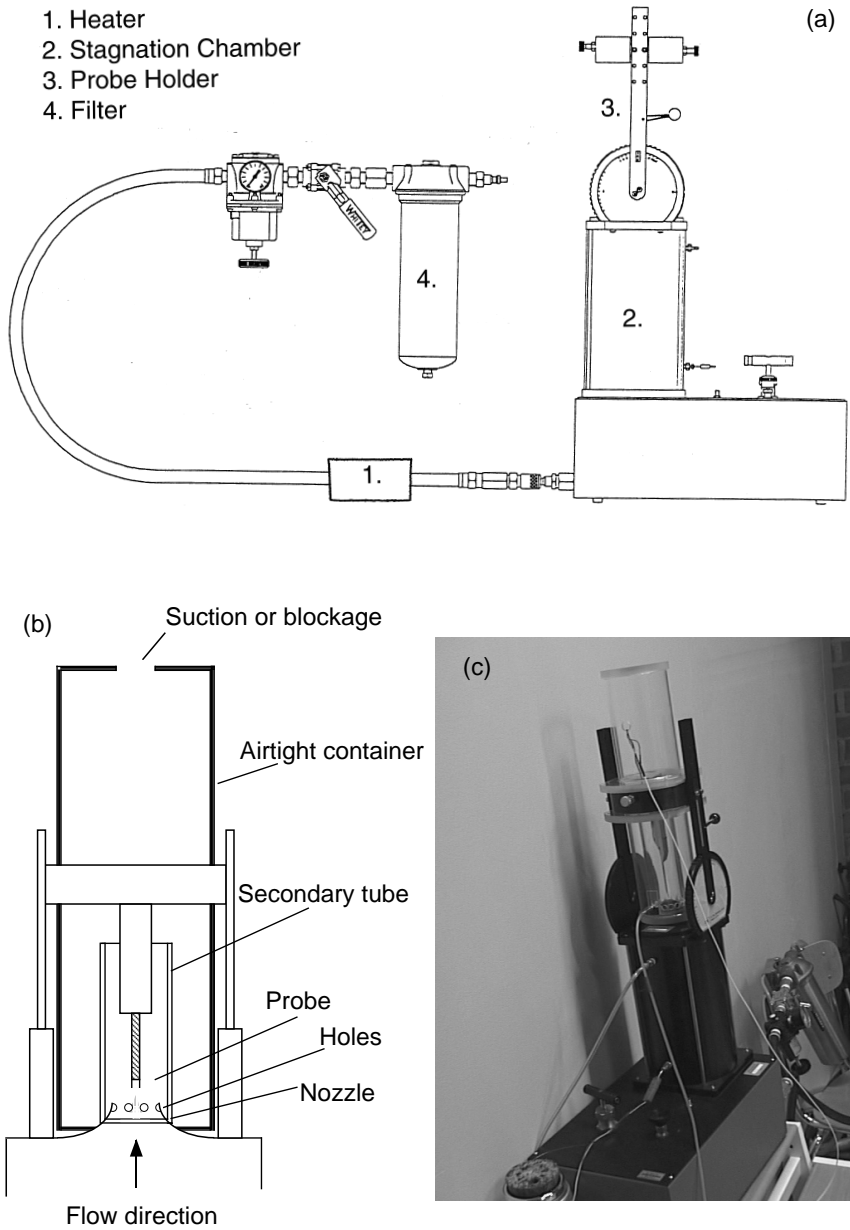
Secondary tube

Probe

Holes

Nozzle

Flow direction

(c)

FIGURE 4.1. The hot-wire calibrator unit. (a): the calibrator unit, (b): the probe-holder arrangement, (c): a photograph of the setup.
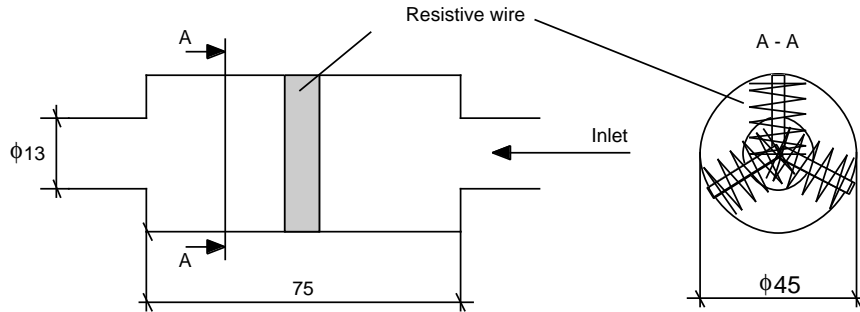
34

FIGURE 4.2. A schematic of the heater. A resistive wire is coiled inside a tube where the air flows towards the stagnation chamber.
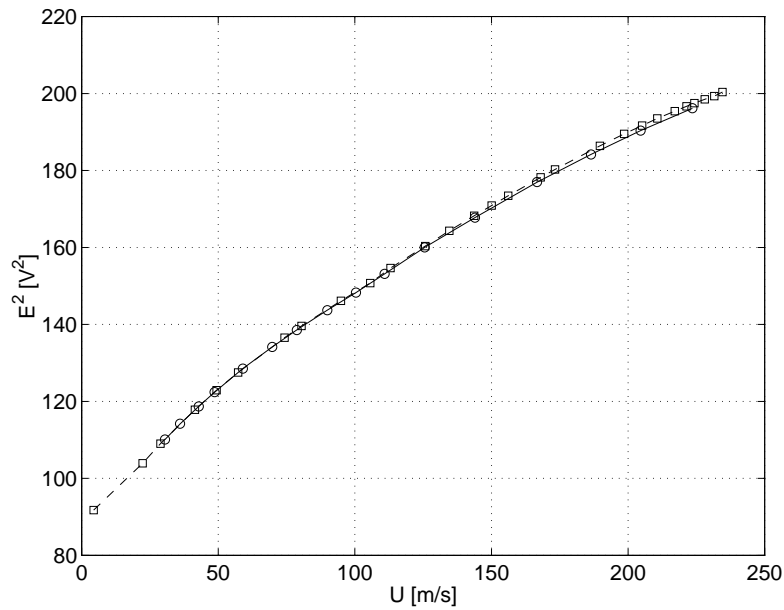

FIGURE 4.3. A classic calibration curve. On the ordinate the anemometer output voltage squared is plotted and on the abscissa the velocity. The squares are the values for the 6 mm diameter nozzle and the circles mark the values for the 3 mm diameter nozzle.

The heated part of the probe consisted of a tungsten wire with a diameter of 5 μm and a length of approximately 1 mm, which was welded between the prongs. Tungsten is preferably used in high velocity flows since tungsten is much stronger than platinum which is the other material typically used for

hot-wire probes. In contrast to platinum wires, which usually are soldered to the prongs, tungsten is not possible to solder and needs to be welded. The length to diameter ratio is larger than 200, which is usually set as a lower limit in order for heat transfer to the prongs to be negligible. The anemometer was a DISA 55 M10 constant temperature anemometer.
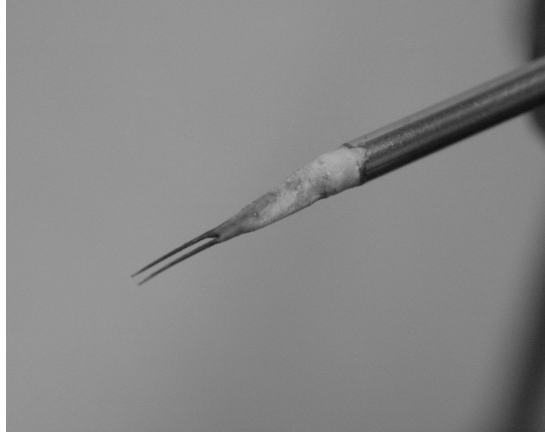

FIGURE 4.4. A hot-wire probe used in the present study.

The welding is done under a microscope where the probe is fixed. With the probe fixed the wire is traversed with micro manipulators so that the wire is lightly resting on top of the prongs. Then the welding electrode is micro manipulated on to the wire pressing it slightly to the prong and a short pulse current is let through, which welds the wire onto the prong. The wire is welded to each prong with two welding spots.

The downside with this welded hot-wire probe with a 5 μm welded tungsten wire, is that it requires a considerable warm up time. It has to be "burned" before the measurements can begin. This is most crucial when the calibration is taking place outside the wind-tunnel, when also the anemometer needs to reach thermally stable conditions. For the DISA 55 M10 anemometer this start up time, including the warming of the anemometer, was empirically determined to about one hour.

4.2.3. *The calibration procedure*

As can be seen in eq. (4.6), the functions $A(M, T_0)$, $B(M, T_0)$ as well as the exponent n should be found for different values of ρU. This is done by placing the hot-wire in a jet, where the velocity, stagnation temperature and the density in the jet can be varied independently. The calibration is then performed in steps where two variables are kept constant while the third is varied.

For instance, by changing the static pressure in the jet the density can be varied, while keeping the Mach number and stagnation temperature constant.

Repeating this for different Mach numbers, the dependence of $A(M)$ and $B(M)$ can be found. Changing the stagnation temperature and repeating the above procedure, the unknown functions can then be determined. The calibration procedure used can be summarized as

1. Set the stagnation temperature.
2. Set the Mach number (given by the pressure ratio between the outlet and the stagnation chamber).
3. Vary the density by applying suction or blockage.
4. Repeat step 3 for the desired Mach numbers.
5. Repeat step 2 and step 3 for different stagnation temperatures.

4.2.4. Calculation procedure

To transform a measured voltage into a velocity the following method was used. Starting from the perfect gas law

$$p = \rho RT \tag{4.7}$$

where R is the specific gas constant. With the definition of the Mach number

$$M = \frac{U}{a} \tag{4.8}$$

where the speed of sound is written as

$$a = \sqrt{\gamma RT} \tag{4.9}$$

Assuming adiabatic flow, the relation of the stagnation temperature and the temperature can be expressed in terms of the Mach number as

$$\frac{T_0}{T} = 1 + \frac{\gamma - 1}{2} M^2 \tag{4.10}$$

The relations (4.8)–(4.10) are inserted in the perfect gas law, eq. (4.7), to get an expression for the mass flux in terms of the static pressure, the Mach number and the stagnation temperature.

$$\rho U = pM \sqrt{\frac{\gamma(1 + \frac{\gamma-1}{2}M^2)}{RT_0}} \tag{4.11}$$

With the above expression and King's law for compressible flow, eq. (4.6), the Mach number can now be calculated from a single voltage if the static pressure, p, and the stagnation temperature are known.

If the definition of the Mach number, eq. (4.8), is rewritten in terms of stagnation temperature with eq. (4.10) as

$$M = \frac{U}{\sqrt{\gamma RT_0 - \frac{\gamma-1}{2}U^2}} \tag{4.12}$$

then the velocity can be calculated implicitly from the Mach number, with the assumption that the flow is adiabatic.

4.2.5. *Derivation of the sensitivity coefficients*

In compressible flow the hot wire is sensitive to several different quantities and this is reflected not only in the mean but also in the fluctuations. A common way of analyzing the response of hot wires in subsonic compressible flows has been to use a linearised expression of the heat transfer law, *e.g.* eq. (4.4), Steinback & Nagabushana (1994). By logarithmically linearizing the heat transfer law, the fluctuations in the voltage, e, can be expressed in terms of the independent variables, density, r, velocity, u, and stagnation temperature, t_0 as

$$\frac{e}{E} = S_\rho \frac{r}{\rho} + S_u \frac{u}{U} + S_t \frac{t_0}{T_0} \tag{4.13}$$

where capital letters are the mean values and the *sensitivity coefficients* are defined as

$$S_\rho = \left. \frac{\partial \ln E}{\partial \ln \rho} \right|_{U,T_0} \tag{4.14}$$

$$S_u = \left. \frac{\partial \ln E}{\partial \ln U} \right|_{\rho,T_0} \tag{4.15}$$

$$S_t = \left. \frac{\partial \ln E}{\partial \ln T_0} \right|_{\rho,U} \tag{4.16}$$

The sensitive coefficients, can be obtained from eq. (4.6) as

$$S_\rho = \frac{n}{2}\left[1 - \frac{A}{E^2}\right] \tag{4.17}$$

$$S_u = S_\rho \left[1 + \frac{1}{nB}\frac{\partial B}{\partial \ln U}\right] + \frac{1}{2E^2}\frac{\partial A}{\partial \ln U} \tag{4.18}$$

$$S_t = \frac{T_0}{2E^2}\left[\frac{\partial A}{\partial M}\frac{\partial M}{\partial T_0} + \frac{\partial A}{\partial T_0}\right] + \frac{T_0}{2B}\left[1 - \frac{A}{E^2}\right]\left[\frac{\partial B}{\partial M}\frac{\partial M}{\partial T_0} + \frac{\partial B}{\partial T_0}\right] \tag{4.19}$$

The partial derivative $\frac{\partial M}{\partial T_0}$ can be found from eq. (4.12) to be

$$\frac{\partial M}{\partial T_0} = \frac{-\gamma RU}{2\left(\gamma RT_0 - \frac{\gamma-1}{2}U^2\right)^{\frac{3}{2}}} \tag{4.20}$$

This approach is based on a linearised theory and only valid for small fluctuations, or if the fluctuations in voltage are related to flow fluctuations by power laws. Another assumption is that the dynamic sensitivities are equal to the static sensitivities, that are found in the calibration process, and the

calibration is made in a steady stream. There have also been different opinions regarding if the velocity and density sensitivities are equal or not. Horstman & Rose (1977) were the first to propose this equality. But Steinback & Johnson (1983) deduced that this was not the case. However the equality has been used anyway Qi-lin & Chang-an (1993).

4.3. Calibration results

4.3.1. *The calibration function*

To determine the calibration function, the anemometer output voltage, E, was measured for different mass fluxes, ρU, at constant Mach numbers, M, and stagnation temperatures, T_0. In each calibration set the stagnation temperature was chosen and kept constant through the set of calibration data. For each stagnation temperature the Mach number was kept constant and the pressure changed in order to change the density, *i.e.* the massflux. This were performed for the Mach numbers 0.2, 0.3, 0.4, ..., 0.9.

The calibration was performed for the stagnation temperatures 21, 25, 28, 32 and 35.5°C. The variation in temperature was less than 0.5 K during the calibration process. For the stagnation temperature 35.5°C measurements were only performed for the Mach numbers 0.5 to 0.9. The overheat ratio was set to 1.5.

In figure 4.5, $\sqrt{\rho U}$ is plotted against the square of the anemometer output in accordance with King's law for compressible flow, eq. (4.6). In the figure the Mach number is constant along each line. The lines in the figure are linear least square fits to the data. Here the exponent n is chosen to one half as originally suggested by King.

The slope of the least square fits are the B function values for the constant Mach number, and the intercept of the lines with the y-axis are the A function values. The A and B values for the different Mach numbers in the range 0.2 to 0.9 are plotted in figure 4.6. The lines are determined by a least square polynomial fits of order four. $A(M)$ varies with a factor 2 in the range $M = 0.2$ to $M = 0.9$, while $B(M)$ remains almost constant. The other temperatures (not shown) are found in between these lines.

The square on the y-axis mark E_0^2, the A value in the incompressible limit. Noticeable is that when the Mach number approaches zero, *i.e.* when the compressible effects becomes negligible, $A(M)$ approaches E_0^2 which is used for incompressible flow.

Using the A and B values for the different Mach numbers and stagnation temperatures and fitting a fourth order least square polynomial in the Mach number and stagnation temperature as the $A(M, T_0)$ and $B(M, T_0)$ functions, the calibration is finished.

Figures 4.7(a) and (b) show $A(T_0)$ and $B(T_0)$ for the different Mach numbers. As can be seen in the figures, $A(T_0)$ is an increasing function for all Mach numbers while $B(T_0)$ is a decreasing function. The figures also show that the
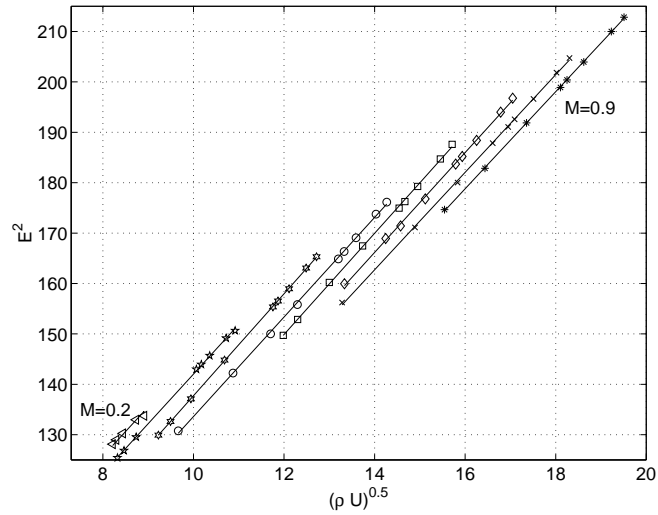
FIGURE 4.5. The anemometer voltage for different values of the mass flux. The stagnation temperature is $21°C$. The Mach number is constant along each line and the lines are linear least squares fitted to the calibration data.
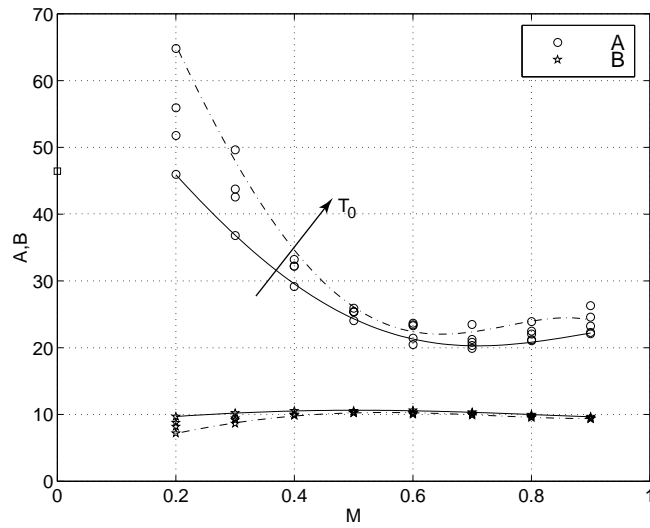

FIGURE 4.6. The functions A and B for different stagnation temperatures. The square on the y-axis mark E_0^2 at $T_0 = 21°C$. (——): $T_0 = 21°C$, (—·—·—): $T_0 = 32°C$
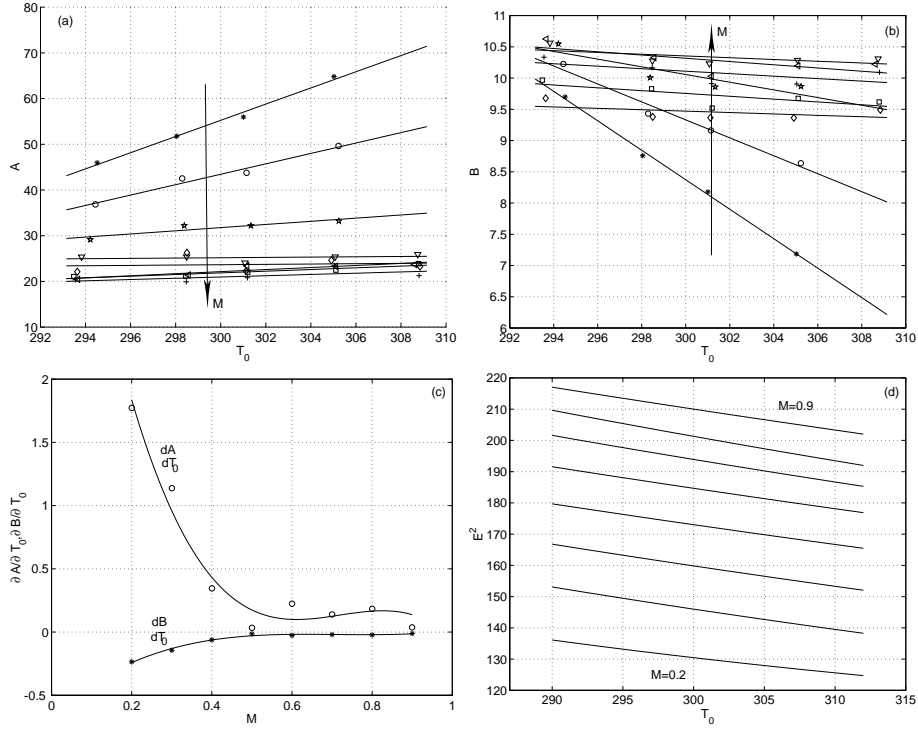
FIGURE 4.7. The temperature dependence of the functions (a): A and (b): B. In the figure the symbols mark constant Mach numbers M: ($*$) M=0.2, ($\circ$) M=0.3, ($\star$) M=0.4, ($\triangledown$) M=0.5, ($\triangleleft$) M=0.6, ($+$) M=0.7, ($\square$) M=0.8, ($\diamond$) M=0.9. The lines are best least square fits to the data points. (c): The temperature differentials of A ($\circ$) and B ($\star$), *i.e.* the slope of the lines for the different Mach numbers in (a) and (b). (d): E^2 plotted against T_0 for the different Mach numbers, the Mach number is increasing upwards.

wire is as most temperature sensitive for low Mach numbers. An explanation for this could be that for a fixed stagnation temperature, the static temperature decreases with the Mach number, which means that the local overheat ratio increases. When the overheat ratio increases, the wire becomes less temperature sensitive.

In figure 4.7(c) the differentials $\frac{\partial A}{\partial T_0}$ and $\frac{\partial B}{\partial T_0}$, the slope of the lines in the upper figures, are plotted against the Mach number. As can be seen in the figure the temperature dependence is largest for Mach numbers up to 0.5. Above $M = 0.5$ both differentials are almost constant.

For CTA in supersonic flows the calibration function is independent of the Mach number reducing the functions A and B to functions of the stagnation

temperature only, Smits *et al.* (1983) and the temperature dependence is satisfyingly linear. Looking at figure 4.7 this Mach number independence seems to appear already at Mach numbers of 0.5. The lines in the figure are fourth order least square fit polynomials. The polynomials are used to calculate the total temperature sensitivity coefficient.

In figure 4.7(d), the temperature dependence of the hot wire for the different Mach numbers is plotted. The figure is created by using the calibration function $E^2 = A(M, T_0) + B(M, T_0)\sqrt{\rho U}$ and only varying T_0. The curves are not straight lines in the figure, but the deviations from a straight line are small. The linear temperature correction for CTA is commonly used in incompressible flow, and has been verified by numerous experiments, see for instance Abdel-Rahman *et al.* (1987). The linear and constant slope of the temperature dependence allow a linear temperature correction for changes in the stagnation temperature, between calibration and measurement, or during the measurement.

The fitted polynomials of $A(M, T_0)$ and $B(M, T_0)$ are used in King's law for compressible flow, eq. (4.6), to get the final calibration function for the hot wire. This calibration function is used on the measured values of velocity, density and static pressure determined in the calibration, to get the error of the calibration. The relative error of the calibration is found to be about 0.3 % in the voltage.

4.3.2. *The sensitivity coefficients*

The calibration curves can also be used to obtain the sensitivity coefficients defined by eqs. (4.14)–(4.16).

In the expression for the density sensitivity coefficient, eq. (4.17), it can be seen that S_ρ should approach $n/2$ when the quotient $A/E^2 \to 0$. In figure 4.8(a), S_ρ is plotted and is seen to approach 0.25 when the Mach number increases, which is in agreement with the theoretical expression.

The velocity sensitivity coefficient, eq. (4.18), figure 4.8(b) varies both with the density and the Mach number, however the density variation gets lower when the Mach number increases.

In the incompressible range the quotient S_u/S_ρ should be one, since the functions A and B are constants for incompressible flow conditions. In figure 4.8(c) it can be seen that the ratio approaches near unity when the Mach number approaches zero. deSouza & Tavoularis (1999) found that this quotient approached zero when the Mach number approached unity, indicating the wire becoming a density fluctuation transducer. This is not found in this investigation or as they comment: "not anywhere else in the literature".

The total temperature sensitivity coefficient, eq. (4.19), figure 4.8(d), is always negative, but approaches zero for the higher Mach numbers showing that the probes become less temperature sensitive for high Mach numbers. The values for $M = 0.2$ does not seem to follow the trend set by the other Mach numbers, but the values for $M = 0.2$ comes from a fit with few points
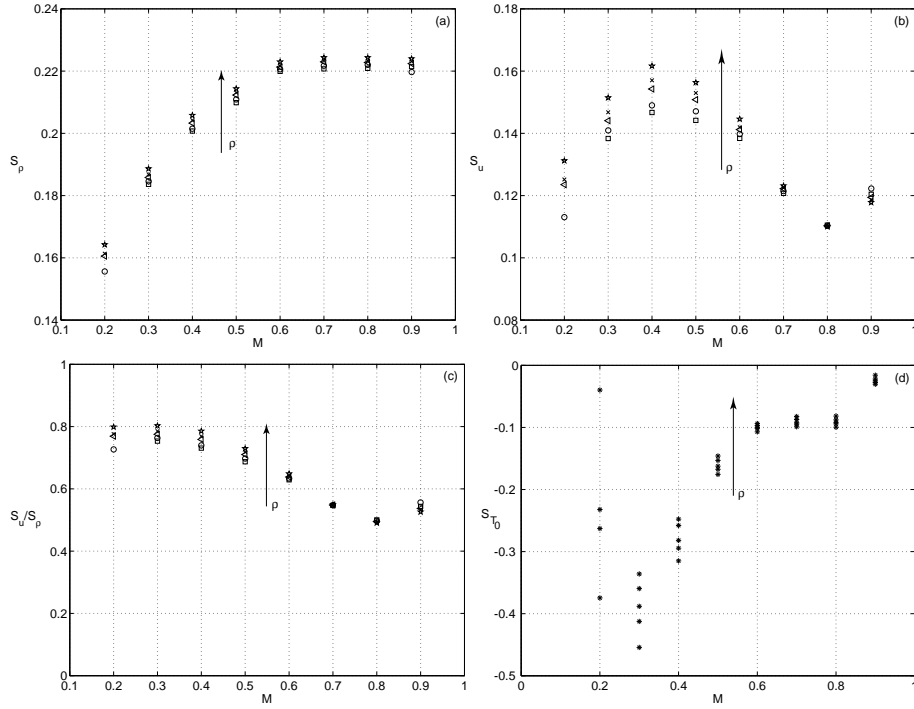
FIGURE 4.8. (a): the density sensitivity coefficient, (b): the velocity sensitivity coefficient, (c): The quotient S_u/S_ρ, (d): the total temperature sensitivity coefficient. The different symbols mark different static densities.

in a small interval, which means that the uncertainty for $M = 0.2$ is relatively large.

CHAPTER 5

Results

5.1. Results from the hot-wire measurements

The hot-wire measurements of the boundary layer was made on the floor at the entrance of the test section. The calibration procedure is the one described in section 4.2. To be able to verify the calibration with respect to the variations in mass flux the measurements were made for three different static pressures and three different Mach numbers, ranging from subsonic to transonic, see table 5.1 for a summary. The pressures were constant within 0.7%. The stagnation temperature was set to 30°C and was kept constant within 0.4 K (0.1%) during the measurements and the hot wire was operated at an overheat ratio of 1.5.

case:	1	2	3	4	5	6	7	8	9
M_∞:	0.3	0.3	0.3	0.5	0.5	0.5	0.7	0.7	0.7
p_s [kPa]:	100	92	110	100	90	110	100	90	110

TABLE 5.1. Overwiev of the measurements

In figure 5.1 the nine measured velocity profiles normalized with the freestream velocity and the incompressible displacement thickness are shown. As can be seen it is possible to reach velocities even lower than 40 % of the freestream velocity, which corresponds to $y < 0.1$ mm from the plate surface. With the normalisation in figure 5.1 the collapse of the profiles is fairly good. The Van Driest transformation eq. (2.67) gives a maximum change of less than 2 % in the velocity and would not considerably change the velocity profiles.

In table 5.2 the shape factor and the displacement thickness and the momentum loss thickness can be found. The parameters have been calculated with both the compressible definitions, eqs. (2.16) – (2.17) and with the incompressible assumption of constant density in the boundary layer. The temperature distribution and thereby the density distribution was assumed to follow Walz' relation, eq. (2.46). The striking fact is that the displacement thickness varies up to 12 % dependent on the method of calculation while the momentum loss thickness is fairly constant. This results in different trends for the shape factor with the Reynolds number based on the momentum loss thickness. The compressible shape factor increases with Reynolds number while the incompressible one decreases. This is consistent with what is found for the laminar case discussed in section 2.2.4.
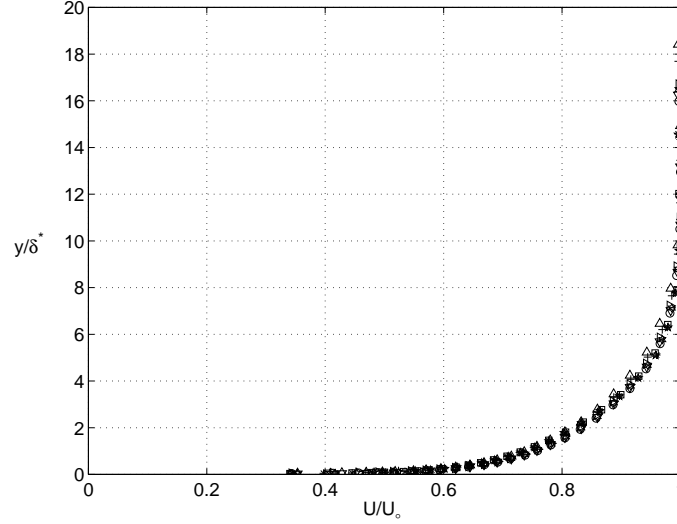
FIGURE 5.1. The velocity profiles for the nine different cases.

case	δ_c^* [mm]	θ_c [mm]	H_c	δ_i^* [mm]	θ_i [mm]	H_i
1	1.46	1.07	1.37	1.42	1.08	1.32
2	1.46	1.07	1.37	1.43	1.08	1.33
3	1.43	1.05	1.37	1.41	1.06	1.33
4	1.29	0.92	1.40	1.22	0.94	1.30
5	1.33	0.94	1.41	1.25	0.97	1.30
6	1.31	0.93	1.40	1.24	0.96	1.30
7	1.20	0.79	1.52	1.06	0.83	1.28
8	1.27	0.83	1.53	1.12	0.87	1.28
9	1.15	0.78	1.48	1.04	0.82	1.27

TABLE 5.2. The shape factor calculated with both the compressible method and the incompressible method.

The errors found, when comparing the free-stream velocity measured with the stagnation pressure tube, and the free-stream velocity derived from the hot-wire voltages are found in table 5.3, in the column "Error". The errors are within 4 % and the calibration are considered satisfactory.

The skin friction coefficient was determined with the Clauser method. Comparing the values with the relation found by Österlund (1999) investigating incompressible zero pressure gradient flat plate boundary layers, the skin friction coefficient seems to follow the same relation, figure 5.2. The skin friction in the same setup was measured by Tillmark (2001) with the oil drop
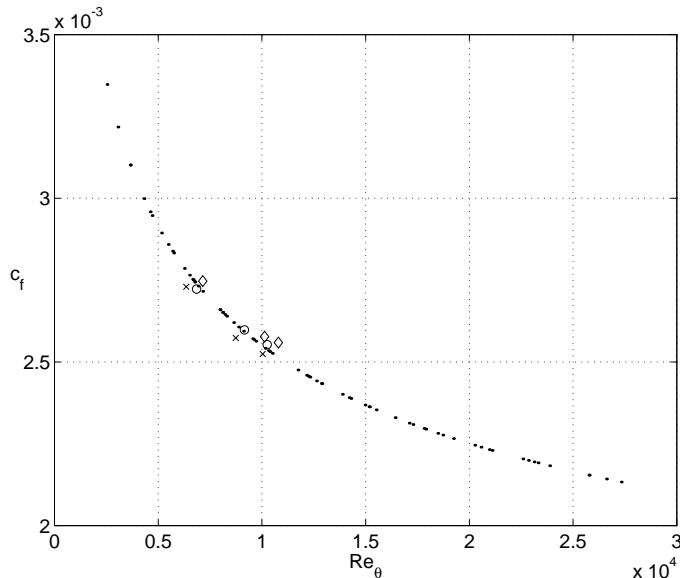
FIGURE 5.2. The skin-friction coefficient plotted against the Reynolds number based on the momentum loss thickness. The symbols are the present mesurements while the dots are the values from Österlund (1999).

method for the Mach numbers $M_\infty = 0.3$, $M_\infty = 0.5$ and $M_\infty = 0.7$ and stagnation temperature $T_0 = 30°C$. The values found is summarized in table 5.3 in the column τ_w^{NT}, the values seems to correspond fairly well with the values determined from the Clauser method. The Fizeau fringes were not very clear and not too many fringes appeared on the photos for the Mach numbers 0.5 and 0.7. But the values found can be used as a guideline.

In figures 5.3 and 5.4 the boundary layer profiles are plotted in inner and outer scales. The profiles collapse nicely with the incompressible law of the wall, but the intercept for the measured profiles is slightly higher than determined by Österlund (1999), the dashed line. The intercept here is 4.6 for the $M = 0.3$ and 5.0 for $M = 0.7$, see table 5.4. Österlund (1999) found the value 4.08 in his low-speed incompressible experiment.

Performing the Van Driest transformation, eq. (2.65), the velocity profiles are shifted upwards, *i.e.* the intercept increases. As can be seen in table 5.4 the compressibility effects are not detectable for the lowest Mach number but is seen to increase with the Mach number.

In figure 5.5 the distributions of turbulent intensity, $u_{rms} = \sqrt{\overline{u''^2}}$, are plotted in inner and outer scaling. In the figures the intensity profiles are plotted together with an incompressible profile measured by Österlund (1999). For the incompressible case a clear peak is found near the wall. As can be

case	Re_θ	Re_x	$\tau_w[\text{Pa}]$	τ_w^{NT}	U_∞^{hw} [m/s]	U_∞^p [m/s]	Error [%]
1	6900	$1.4 \cdot 10^6$	19	17	105.9	108.5	2.4
2	6900	$1.4 \cdot 10^6$	17	-	103.2	106.2	2.5
3	6700	$1.4 \cdot 10^6$	20	-	103.3	106.2	2.5
4	9000	$2.2 \cdot 10^6$	44	48	169.0	170.7	1.4
5	9300	$2.2 \cdot 10^6$	41	-	171.6	172.8	1.1
6	9300	$2.2 \cdot 10^6$	50	-	170.0	172.6	1.7
7	9800	$3.0 \cdot 10^6$	78	86	233.6	227.8	2.2
8	10400	$3.0 \cdot 10^6$	71	-	234.8	229.6	1.4
9	9600	$3.0 \cdot 10^6$	85	-	234.7	226.3	3.5

TABLE 5.3. Results from the measurements. U_∞^{hw} and U_∞^p are the freestream velocities measured with the hot wire and the stagnation pressure probe respectively.
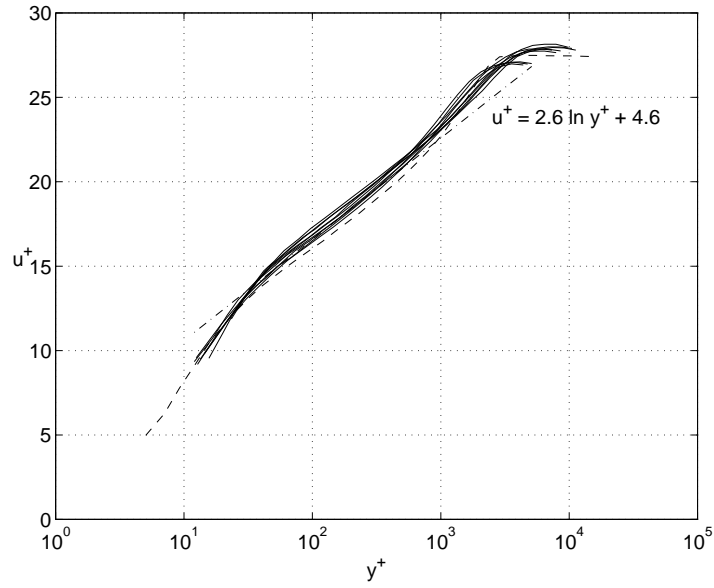

FIGURE 5.3. The velocity profiles in inner scaling. The dashed line is an incompressible velocity profile measured by Österlund (1999).

seen for the present measurements in the inner part of the boundary layer the fluctuations are low and no peak close to wall is found. This is due to the fact that the wire length is too large to resolve small turbulent scales. The size of the probe in viscous scales can be found in table 5.5. A too long probe works as a spatial low-pass filter and therefore measure too low fluctuation
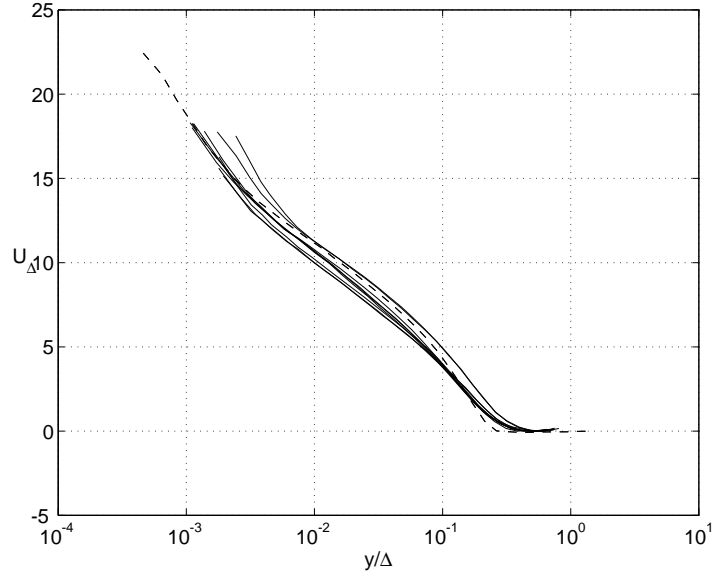
5. RESULTS

FIGURE 5.4. The velocity profiles in outer scaling

case:	$1-3$	$4-6$	$7-9$
C:	4.6	4.6	5.0
B:	4.6	4.7	5.2

TABLE 5.4. The intercept for the law of the wall. C is the untransformed intercept and B the Van Driest transformed intercept.

levels. Nevertheless the *rms*-profiles show a good agreement in the outer region whereas large discrepancies are seen close to the wall.

case:	$1-3$	$4-6$	$7-9$
l^*:	260	410	540

TABLE 5.5. Hot-wire length in viscous units.

When u_{rms} is determined usually the strong Reynolds analogy is used to determine the temperature fluctuations as: $T_{rms}/\overline{T} = (\gamma - 1)M_\infty^2 u_{rms}/\overline{u}$. If the perfect gas law is time averaged and assuming $|\overline{\rho''T''}| \ll \overline{\rho}\overline{T}$, then

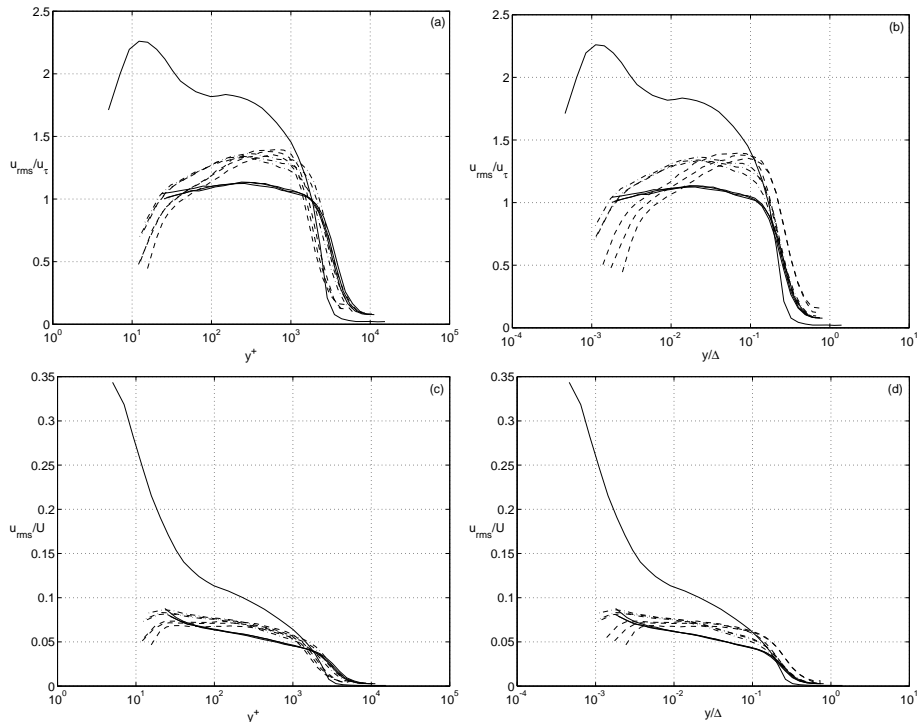$$\frac{p''}{\overline{p}} = \frac{\rho''}{\overline{\rho}} + \frac{T''}{\overline{T}}. \tag{5.1}$$

FIGURE 5.5. (a) and (c): u_{rms} in inner scaling. (b) and (d): u_{rms} in outer scaling. In the plots the line that deviates is an incompressible intensity profile from Österlund (1999). $(--)$ $M = 0.3$, $(- \cdot -)$ $M = 0.5$, and $(—)$ $M = 0.7$.

Generally the assumption is that, the pressure fluctuations are small compared to the density and temperature fluctuations, Kistler (1959), leaving

$$\frac{\rho''}{\overline{\rho}} \approx -\frac{T''}{\overline{T}}. \tag{5.2}$$

With the above relations the temperature and density fluctuations can be derived from the velocity fluctuations with the assumption of negligible pressure fluctuations and that the strong Reynolds analogy holds. This has only been performed for the free-stream values, table 5.6, since the turbulence intensity distributions are underestimated in a large part of the boundary layer, figure 5.5.

The third, *skewness*, and fourth, *flatness*, moments of the probability density function can be found in figure 5.6. These higher moments are defined as:

case:	U_∞ [m/s]	T_∞ [K]	ρ_∞ [kg/m³]	$100\frac{u_{rms}}{u_\infty}$	$1000\frac{T_{rms}}{T_\infty}$
1	108.5	298.2	1.18	0.44	0.17
2	106.2	297.1	1.10	0.58	0.22
3	106.2	298.4	1.30	0.44	0.17
4	170.7	289.5	1.22	0.34	0.34
5	172.8	288.9	1.10	0.35	0.36
6	172.6	289.2	1.34	0.34	0.34
7	227.8	278.2	1.27	0.29	0.54
8	229.6	277.6	1.14	0.28	0.53
9	226.3	278.7	1.39	0.28	0.50

TABLE 5.6. Table of freestream values

$$S_u = \frac{\overline{u''^3}}{\overline{u''^2}^{3/2}} \quad (5.3)$$

$$F_u = \frac{\overline{u''^4}}{\overline{u''^2}^2} \quad (5.4)$$

The skewness describes the asymmetry of the signal and is dominated by the tails of the probability density function. A negative skewness indicates that negative deviations dominate the signal. For the flatness, the tails are even more weighted and both positive and negative deviations give contributions of the same sign. A high flatness indicates a high intermittency in the signal. For a Gaussian signal, the skewness is zero and the flatness is three. As can be seen in figure 5.6 this behaviour can be found in the free stream for both the flatness and skewness. However the validity of the S_u and F_u profiles must be questioned in the inner part of the layer where the turbulence is dominated by smaller scales, since the wire length is fairly large. As can be seen in figure 5.6, the skewness is around zero and the flatness around three in the inner part indicating a Gaussian turbulence distribution. In the outer part where the errors from the probe is less significant the familiar peak in the flatness profile, and the dip in the skewness profile, are found. The magnitudes of the peak and dip appear to be a little low. A skewness of -1.4 is found in this investigation. Österlund (1999) found for the incompressible layer a value of around -3.5. The same can be said for the flatness, here values of five to seven is found while Österlund (1999) measured values well above ten.

In figure 5.7 the velocity signal for case 6 is plotted for three different positions in the boundary layer, a point in the buffer region, $y^+ = 15$, at a position in the logarithmic region, $y^+ = 280$, and at a position in the wake region $y^+ = 4560$. It can be seen that the fluctuations increase from $y^+ = 15$ to $y^+ = 280$. The signal for $y^+ = 4560$ show the high skewness with the dips in the signal, which is assumed to be blobs of low speed boundary layer fluid that pass the probe.
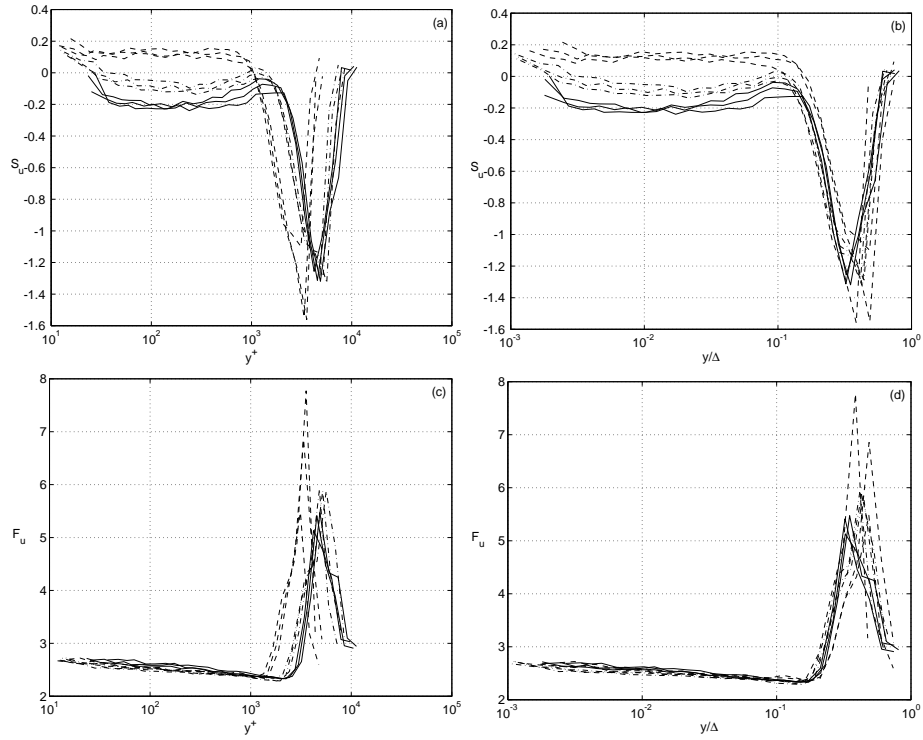
FIGURE 5.6. The skewness in inner, (a), and outer scaling, (b), and the flatness in inner, (c), and outer, (d), scaling. $(--)$ $M = 0.3$, $(- \cdot -)$ $M = 0.5$, and $(—)$ $M = 0.7$.
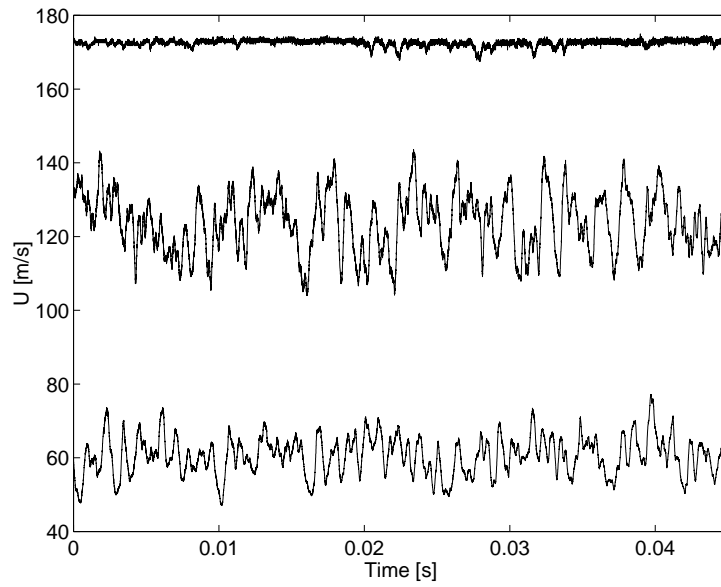
FIGURE 5.7. The velocity signal for case 6, at three different positions in the boundary layer. Top signal: $y^+ = 4560$. Middle signal: $y^+ = 280$. Lower signal: $y^+ = 15$

5.2. Results from the PIV measurements

5.2.1. *The PIV measurements*

PIV measurements have been performed at free-stream Mach numbers ranging from 0.30 to 0.70, at different positions on a bump model in the test section. The different measurement areas are shown in figure 5.8 and table 5.7. The PIV system have been operated both in cross-correlation and auto-correlation mode, see table 5.8. The free-stream stagnation pressure was measured with a stagnation pressure probe in the stagnation chamber and the static pressure was measured both at the inlet and outlet of the test section. The stagnation temperature was assessed with a copper-constantan thermocouple to 30°C ± 0.4 K in all measurements. The free stream Mach number at the inlet of the test section was determined from the inlet static pressure and the free-stream stagnation pressure.
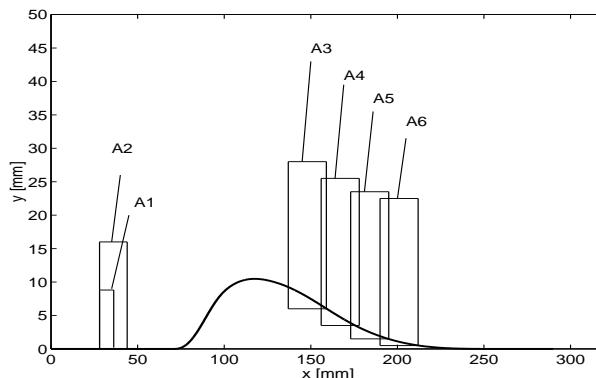

FIGURE 5.8. The positions of the measurement areas. For the mode of operation see table 5.8. The curvature of the bump begins at $x = 70$ mm and the highest point on the bump is located at $x = 117.5$ mm. (Junction between model and inlet channel floor at x=0)

area:	A1	A2	A3	A4	A5	A6
x [mm]:	28-36.2	28-44	137-159	156-178	173-195	190-212
y [mm]:	0-8.2	0-16	6-28	3.5-25.5	1.5-23.5	0.5-22.5

TABLE 5.7. Overview of dimensions and positions of the measurement areas.

The number of images/image pairs was 1100 in all cases. The flow was seeded with oil particles into the boundary layer in the stagnation chamber. The particles were generated by a spray-atomizer delivering particles with a diameter of about 0.2 μm, according to the manufacturer (Polytech (1997)).

5. RESULTS

The conventional validation criterias were used in all measurements, namely that the particles should not have travelled further than 25 % of the interrogation area side-length and a peak value ratio of 1.20. The interrogation areas were 50 % overlapped. The interrogation area size were 64×64 pixels in all measurements except for the measurements in area A2 at freestream Mach number 0.30, where the interrogation area size was 32×32 pixels. The time interval between the images was set according to eq. (3.4).

Area	Mode	Image size [mm]	*ia* sidelength [mm]	M_e
A1	a-c	8.2×8.2	0.284	0.69
A2	c-c	16×16	0.256	0.30
A2	c-c	16×16	0.504	0.50
A2	c-c	16×16	0.504	0.70
A3	c-c	22×22	0.688	0.69
A4	c-c	22×22	0.688	0.69
A5	c-c	22×22	0.688	0.69
A6	c-c	22×22	0.688	0.69

TABLE 5.8. Overwiev of the measurements. a-c stands for auto-correlation and c-c cross-correlation. *ia* is short for interrogation area.

5.2.2. *PIV results and discussion*

5.2.2.1. *Inlet conditions*

The streamwise velocity in the turbulent boundary layer at area A2 was measured in order to be able to compare data obtained with different methods. The measurements were performed at free stream Mach numbers 0.30, 0.50 and 0.70. The inlet static pressure was atmospheric, the same as for one of the operating points for the hot-wire measurements. Figure 5.9 shows the velocity profiles in the inlet region obtained from PIV and from previous hot-wire data. The hot-wire measurements were performed on a flat plate model 10 mm upstream of the junction between the plate and the inlet tunnel floor, whereas the PIV measurements were carried out 28 mm downstream of the junction due to optical access limitations. The figure contains both shifted and unshifted velocity profiles to facilitate comparisons between different Mach numbers as well as different methods. The velocity is normalised with the free-stream value and the wall normal coordinate is normalised with the displacement thickness determined by assuming constant density in the boundary layer.

The figure shows an overall good agreement between hot-wire and PIV data for the two highest Mach numbers investigated (comparison in (D)) though the PIV profiles are slightly less blunt. The major difference between the methods is found at the lowest Mach number, $M_e = 0.3$ (profile (A)), where PIV data gives a higher velocity compared with the hot-wire but also compared
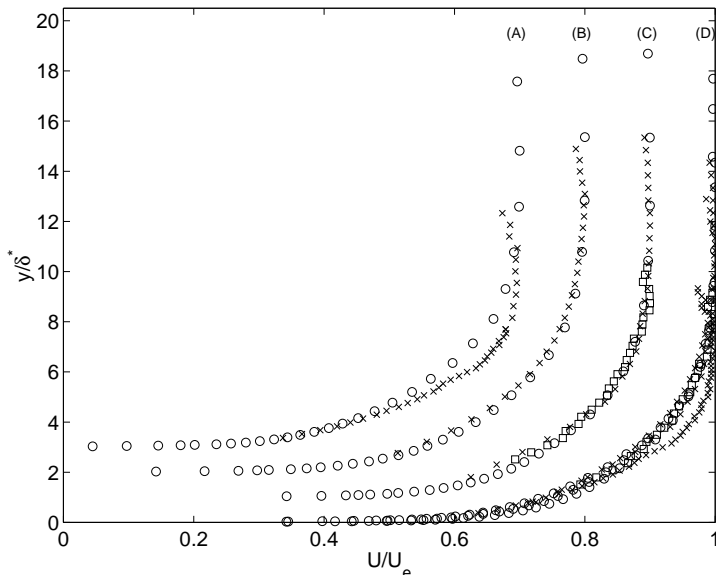
FIGURE 5.9. Velocity profiles at the inlet of the test section for different free-stream Mach numbers. The figure contains profiles shifted both to the left and upwards in steps of 0.1 and 1 respectively (A: $M_e = 0.3$), (B: $M_e = 0.5$), (C: $M_e = 0.7$) and unshifted (D). ($\circ$) are data from hot-wire measurements and ($\times$) data from PIV measurements. ($\square$) shows measurements at $M_e = 0.69$ with the PIV system in auto-correlation mode.

to profiles obtained at higher Mach numbers. The profile was obtained using 32×32 pixels interrogation areas compared to 64×64 pixels used in the other PIV profiles. The velocity overestimate is presumably caused by the smaller interrogation area. Decreasing the interrogation area size, fewer particles are present, the signal to noise ratio decreases but also the bias towards a lower velocity becomes prominent with higher velocity. This is believed to be the case though the data points are not exceedingly scattered. The underestimate is most pronounced for the largest velocity, the free stream, *i.e.* the normalizing velocity. As the velocity and hence also the bias effect decreases throughout the boundary layer the normalised velocity profile becomes more blunt compared with the unbiased profile.

Turbulence intensity distributions are also obtained from the PIV data. They are not shown here because the turbulence intensities are approximately three times higher than those measured by the hot-wire throughout the boundary layer and considered not to be realistic. The increase in turbulence is attributed to poor seeding and too few samples.

PIV data

M_e	δ_c^* [mm]	θ_c [mm]	H_c	δ_i^* [mm]	θ_i [mm]	H_i	$Re_{\theta i}$
0.30	1.70	1.28	1.33	1.66	1.28	1.29	7300
0.50	1.19	0.85	1.40	1.12	0.87	1.29	8500
0.70	1.13	0.75	1.51	1.00	0.77	1.30	10300
0.69	0.99	0.65	1.53	0.87	0.67	1.29	8800

Hot-wire data

M_e	δ_c^* [mm]	θ_c [mm]	H_c	δ_i^* [mm]	θ_i [mm]	H_i	$Re_{\theta i}$
0.30	1.46	1.07	1.37	1.42	1.08	1.32	6900
0.50	1.29	0.92	1.40	1.22	0.94	1.30	9000
0.70	1.20	0.79	1.52	1.06	0.83	1.28	9800

TABLE 5.9. Different boundary layer parameters calculated assuming compressible as well as incompressible boundary layer flow.

Displacement thickness, momentum loss thickness, shape factor and Reynolds number have been determined assuming compressible as well as incompressible boundary layer flow. During these calculations PIV data were extended with hot-wire data close to the plate surface where no particle images could be retrieved in the strong glare. The results are given in table 5.9 together with parameters determined in section 5.1. If the data from the measurements for $M_e = 0.3$ are not considered, then the shape factor from the PIV and hot-wire measurements agree within 2 %. The displacement thicknesses and momentum loss thicknesses are all lower for the PIV data (within 8 %). This can be attributed to that the measurements were made at two different occasions, and the experimental facility had been used with other exchangeable test rigs during this period. In the replacement of the wind-tunnel something might have been altered that influence the development of the boundary layer. However, the boundary layer have reached an equilibrium in accordance to that found in the hot-wire measurements.

5.2.3. *Visualisations*

A sequence of four PIV images of area A3 capturing the unsteady shock system at the downstream side of the bump at inlet Mach number 0.69, are shown in figure 5.10. The stagnation pressure is 160 kPa and the static outlet pressure is 105 kPa. The images are selected from the PIV image database and the two first images show the extreme positions of the shock system whereas the other two show intermediate positions. Bright areas in the pictures are mainly scattered light from clusters of seeding particles, condensed water vapour and shock fronts imbedded in the flow. The seeding particles are predominantly found in the lower part of the pictures while the very bright area in the upper part is caused by fog. The bright curves found in the central part of the PIV images point out a lambda shock system. The oblique leading shock C_1
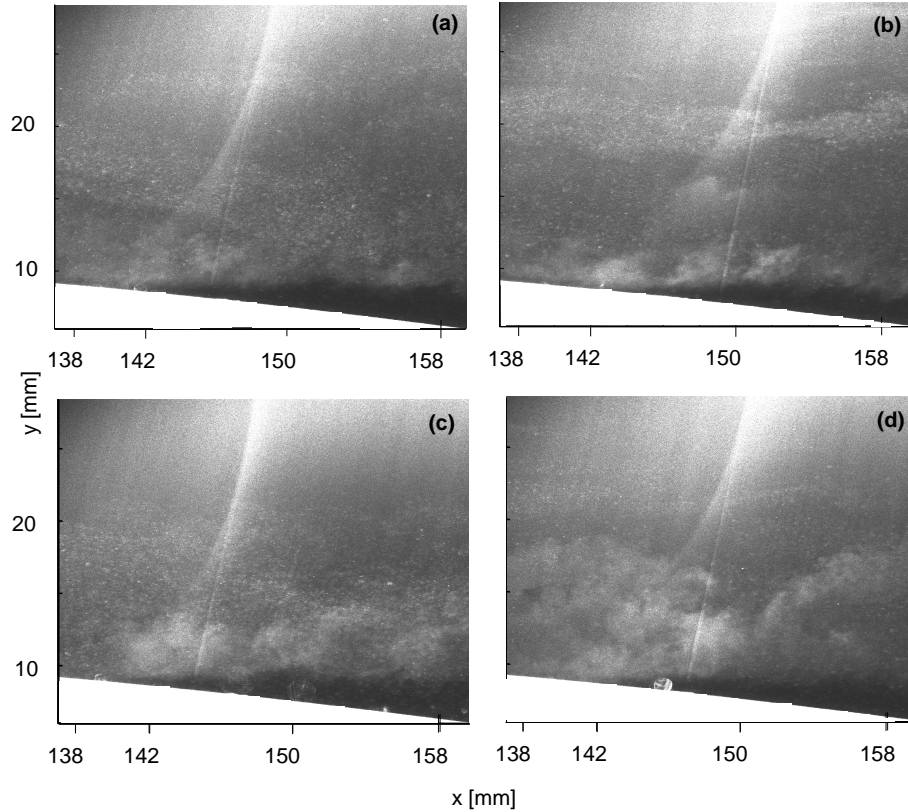
FIGURE 5.10. PIV images of the area covering the shock system. The pictures show the light scattered by groups of particles in the flow as bright areas. The white area in the lower part of the figures is a part of the model. The flow is from left to right. The exposure time is 4 ns.

is hardly visible but is confirmed by schlieren pictures (by Bron (2003)) taken at the same flow conditions, see figure 5.11. The shock system is unsteady and moves randomly back and forth between $x = 142$ mm and $x = 149$ mm, a motion most likely caused by small variations in the upstream and downstream conditions in the flow system. The schlieren pictures show that the flow close to the surface changes drastically downstream of the leading shock foot (C_1), due to either a radical increase in the boundary layer thickness or a separation. The appearance of a lambda shock together with PIV images showing negligible number of particles in the region close to the surface strengthens the presumption of a shock-induced separation.
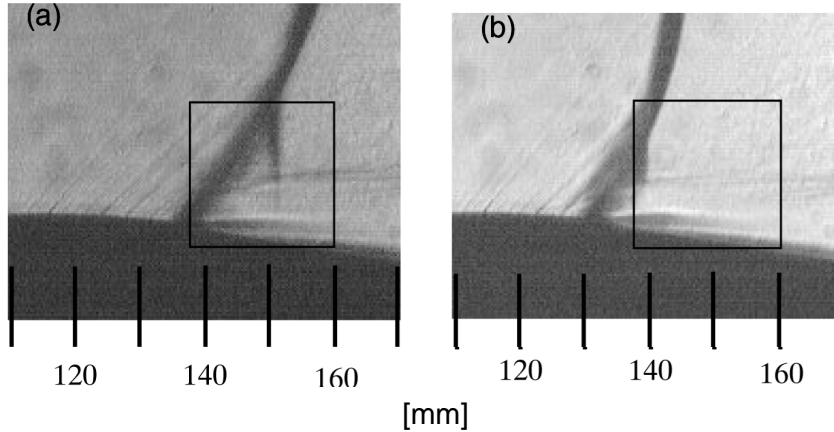
FIGURE 5.11. Schlieren images of the shock wave boundary layer interaction at two different outlet pressures, 104 kPa (a) and 106 kPa (b). The flow is from left to right. Exposure time 1 ms. The black frame encloses the same area as shown in the PIV images. The scale on the x-axis is within ± 1 mm. The images are from Bron (2003), with permission.

5.2.4. Shock wave/boundary layer interaction

The ensemble averaged (1100 frames) Mach number distribution around and across the shock 7 mm above the bump surface is shown in figure 5.12. The figure shows a gradual increase in the Mach number from about 1.25 to 1.27 approaching the shock, a drastic fall in the Mach number entering the shock system and finally a slight recovery to an output Mach number of 0.92 which decreases gradually downstream.

The increase in the Mach number upstream of the shock is caused by the supersonic expansion over the curved bump surface and is verified theoretically using Prandtl-Meyer expansion, shown in the figure as a dashed line. The Mach number distribution in the shock region is an average over an oscillating shock system changing both in strength and position. Assuming a sinusoidal shock motion and a nonlinear relation between shock position and strength gives the general trend but does not explain the dip and recovery in the Mach number at the outlet of the shock system. The explanation is instead sought in a post-shock expansion due to a wall curvature change caused by the sudden increase in the boundary layer thickness. The small final decay in Mach number downstream of the shock system is attributed to subsonic expansion along the bump profile. The downstream Mach number obtained from relations over a normal shock is also included in the figure (full line). Comparison with the measurements show that the lambda shock system is less dissipative and the post-shock Mach number is considerable higher.
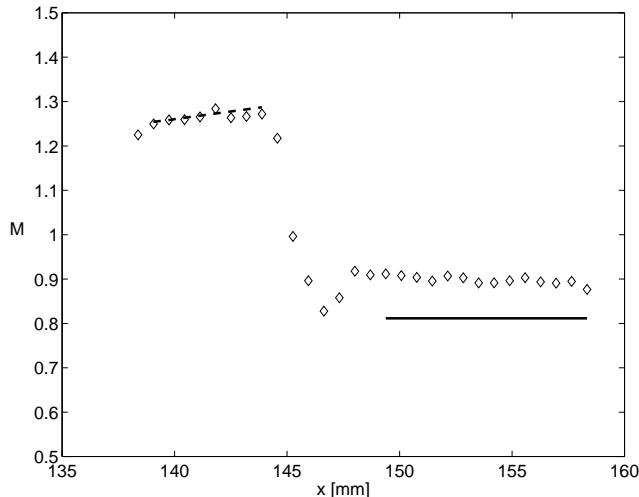
FIGURE 5.12. The Mach number distribution at $y = 7$ mm ($\diamond$) over the surface. ($--$) Prandtl-Meyer theory. ($—$) normal shock relations. The shock system oscillates between $x = 142$ and $x = 149$ mm.

The velocity distribution was measured at a number of positions on the bump, both upstream and downstream of the shock system, see figure 5.13. The normalized velocity profiles are found in figure 5.14.

The velocity profile upstream of the shock, (A), shows a large scatter in the data in the outer part of the boundary layer, compared with the other profiles. This is due to the high light reflectivity of the condensed water vapor, previously mentioned, which reduces the visibility of the seeding thus creating a low signal to noise ratio. Downstream of the shock the velocity data are more coherent and smooth profiles are obtained.

The boundary layer thickness is seen to grow downstream of the shock and the thickness is increased from about 1 mm upstream of the shock (A) to 11 mm approximately 45 mm downstream of the shock (D). The velocity outside the boundary layer decreases slowly as the flow expands along the profile downstream of the shock.

Measurements with the PIV system in auto-correlation mode were also made at several positions with a measuring area of 8.2 mm $\times$ 8.2 mm. However the velocity data were very scattered likely due to lower particle density in the interrogation areas, as discussed earlier, and all profiles but one were discarded. This velocity profile at $x = 138$ mm, upstream of the shock, is shown in the figure and a good agreement with the cross-correlation data is found.

The backflow coefficient *i.e.* the fraction of time the flow is reversed, was determined downstream of the shock and indicates that no separation occurs.
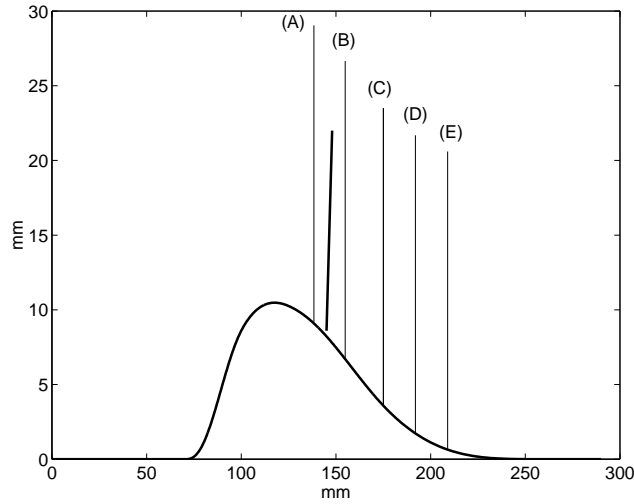
FIGURE 5.13. The locations of the different mean profile measurements shown in figure 5.14. The thick line points out the mean position of the shock. The height of the line indicates the vertical extent of the measuring area. (A) $x = 138$ mm, (B) $x = 155$ mm, (C) $x = 175$ mm, (D) $x = 192$ mm and (E) $x = 209$ mm. The shock system moves between $x = 142$ and $x = 149$ mm.

This is in line with the profiles in figure 5.14 but contradictory to what was proposed from images containing the lambda shock. However a detailed study of the sequence of images used in the determination of the mean profiles shows that the particle density in the region close to the profile surface varies intermittently from particle density similar to that obtained in the freestream to no particles at all. This may indicate a periodic separation not registered because of a lack of particles during these events. The large change in the velocity profile at position (E) in figure 5.14 strengthen the above hypothesis.
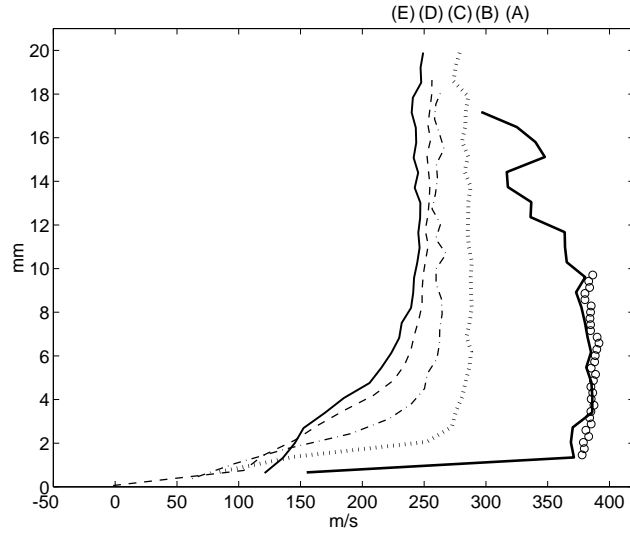
FIGURE 5.14. Mean streamwise velocity profiles upstream and downstream the shock. The vertical distance is measured from the bump surface. (A) $x = 138$ mm, (B) $x = 155$ mm, (C) $x = 175$ mm, (D) $x = 192$ mm and (E) $x = 209$ mm. ($\circ$) are data from measurements in auto-correlation mode at (A). Measurement area 8.2 mm×8.2 mm.

CHAPTER 6

Summary

A calibration unit and methodology were developed for calibration of hot-wire probes in compressible flows. In subsonic compressible flow the calibration function "King's law for compressible flow", $E^2 = A(M, T_0) + B(M, T_0)(\rho U)^n$, is shown to be a suitable generalisation of King's law. The function $A(M)$ is close to E_0^2 when the flow is considered to be incompressible but varies with a factor of about two in the Mach number interval from 0.2 to 0.9 whereas $B(M)$ is found to be essentially constant in the interval. E^2 is found to be a linear function of the stagnation temperature for constant Mach numbers.

Hot-wires were used to measure the flat plate zero pressure gradient turbulent boundary layer at three different static pressures and at three different free-stream Mach numbers. The calibrated hot-wires measured free-stream velocities with an error of about one to three percent in the mean velocity for all static pressures and Mach numbers. The mean velocity profiles were found to follow the incompressible law of the wall for all of the Mach numbers ran. The von Karman constant was found to be 0.39, the same value as for incompressible flow measured by Österlund (1999). The intercept was found to be 4.6 at $M_\infty = 0.3$ and 5.0 at $M_\infty = 0.7$ which is higher than the incompressible value of 4.1 found by Österlund (1999). Using the Van Driest transformation the intercept increased to 5.2 at $M_\infty = 0.7$ while the transformation showed no effect at $M_\infty = 0.3$.

The hot-wire length was found to be too large to resolve the small turbulent scales. However in the outer part of the boundary layer the streamwise turbulence intensity is similar to that of an incompressible boundary layer. The dip in the skewness and peak in the flatness in the outer part of the boundary layer were found to be smaller in magnitude compared to what was obtained in incompressible boundary layer study by Österlund (1999). This may be due to the large hot-wire length but may also be an effect of compressibility.

PIV was also used to measure the boundary layer for the flow over a two dimensional bump at the same Mach numbers as for the hot-wire measurements. The PIV system was operated in both cross- and auto-correlation mode. The data for the inlet boundary layer showed an overall good agreement in the mean velocities compared with the hot-wire measurements. However, strong diffuse light reflections from the surface covered the scattered light from the seeding particles in the measurements close to the surface. It was not possible

to determine the turbulence intensity distributions in the boundary layer due to poor seeding.

The variation of the shape-factor with the Reynolds number was found to differ depending on if the flow was considered incompressible or compressible in the calculations. In the incompressible case the shape-factor decreases whereas it increases in the compressible case. Hence, it has to be clearly stated how the shape factor is calculated.

Velocity profiles were also measured for the transonic flow over the bump model. An oscillating lambda shock wave was found to cause boundary layer separation. The conclusion of a separated boundary layer was not supported by the backflow coefficient, but a boundary layer growth of 10 mm in a distance of 45 mm indicated a separated boundary layer downstream of the shock wave.

Acknowledgements

Bibliography

ABDEL-RAHMAN, A., TROPEA, C., SLAWSON, P. & STRONG, A. 1987 On temperature compensation in hot-wire anemometry. *Journal of physics E: Scientific instruments* **20**, 315–319.

ADRIAN, R. 1991 Particle-imaging techniques for experimental fluid mechanics. *Annu. Rev. Fluid Mech.* **23**, 261–304.

ADRIAN, R. J. & YAO, C. S. 1985 Pulsed laser technique application to liquid and gaseous flows and the scattering power of seed materials. *Applied Optics* **24**, 44–52.

ANGELE, K. P. 2003 Private communication.

BRON, O. 2003 Private communication.

BRUUN, H. H. 1995 *Hot-wire anemometry.* Oxford University Press.

DANTEC 1998 *FlowMap®, Installation and users guide*, 4th edn.

DELERY, J. & MARVIN, J. G. 1986 *Shock wave boundary layer interactions.* AGAR-Dograph 280.

DESOUZA, F. & TAVOULARIS, S. 1999 Hot-wire response in high subsonic flow. *AIAA Paper* **99-0310**, 1–9.

DOLLING, D. S. & MURPHY, M. T. 1983 Unsteadiness of the separation shock wave structure in a supersonic compression ramp flowfield. *AIAA J.* **21**, 1628–1634.

ERENGIL, M. E. & DOLLING, D. S. 1991 Unsteady wave structure near separation in a Mach 5 compression ramp interaction. *AIAA J.* **29**, 728–735.

HINZE, J. O. 1975 *Turbulence*, 2nd edn. McGraw-Hill.

HORSTMAN, C. C. & ROSE, W. C. 1977 Hot-wire anemometry in compressible flow. *AIAA J.* **15**, 395–401.

HUANG, P. G., COLEMAN, G. N. & BRADSHAW, P. 1995 Compressible turbulent channel flows: DNS results and modelling. *J. Fluid Mech.* **305**, 185–218.

INGER, G. R. & SOBIECZKY, H. 1978 Normal shock interaction with a turbulent boundary layer on a curved wall. *VPI aero report.* (088).

JOHNSTON, R. & FLEETER, S. 1997 Compressible flow hot-wire calibration. *Exp. Fluids* **22**, 444–446.

KEANE, R. & ADRIAN, R. 1992 Theory of cross-correlation in PIV. *Applied scientific research* **49**, 191–215.

KING, L. V. 1914 On the convection of heat from small cylinders in a stream of fluid. *Phil. Trans. Roy. Soc.* **A214**.

BIBLIOGRAPHY

KISTLER, A. 1959 Fluctuation measurements in a supersonic turbulent boundary layer. *Phys. Fluids* **2**, 290–296.

KOSINOV, A. D., MASLOV, A. A. & SHEVELKOV, S. G. 1990 Experiments on the stability of supersonic laminar boundary layers. *J. Fluid Mech.* **219**, 621–633.

KOVASZNAY, L. 1953 Turbulence in supersonic flow. *J. Aero. Sci.* **20**, 657–674.

LEE, B. H. K. 1990 Oscillatory shock motion caused by transonic shock boundary-layer interaction. *AIAA J.* **28**, 942–944.

MCDEWITT, J. B., LEVY JR., L. L. & DEIWERT, G. S. 1975 Transonic flow about a thick circular-arc airfoil. *AIAA J.* **14**, 606–613.

MEDICI, D. 1999 *Automatic fringe detection for shear-stress measurements by oil-film interferometry.*. Masters thesis 1999:16, Dept. Mechanics, Royal Institute of Technology, Stockholm.

MELLING, A. 1997 Tracer particles and seeding for particle image velocimetry. *Meas. Sci. Technol.* **8**, 1406–1416.

NANDANAN, M., STANEWSKY, E. & INGER, G. R. 1980 Airfoil flow analysis with a special solution for shock/boundary-layer interaction. *AIAA J.* **19**, 1540–1546.

ÖSTERLUND, J. 1999 *Experimental studies of zero pressure-gradient turbulent boundary-layer flow*. Doctoral thesis 1999:16, Dept. Mechanics, Royal Institute of Technology, Stockholm.

POLYTECH 1997 *Manual for the particul generator L2F-1000A*. Polytech GmbH Waldbronn, Germany.

QI-LIN, Y. & CHANG-AN, Z. 1993 Measurement of turbulent boundary layer in transonic flow. *Chinese journal of aeronautics* **6**, 79–84.

RAGHUNATHAN, S. & MCADAM, R. J. W. 1983 Freestream turbulence and transonic flow over a "bump" model. *AIAA J.* **21**, 467–469.

RAGHUNATHAN, S., MITCHELL, R. D. & GILLAN, M. A. 1998 Transonic shock oscillations on NACA0012 aerofoil. *Shock Waves* **8**, 191–202.

ROSS, C. B., LOURENCO, L. M. & KROTHAPALLI, A. 1994 Particle image velocimetry measurements in a shock-containing supersonic flow. *AIAA Paper* **AIAA-94-0047**, 1–13.

SCHLICHTING, H. & GERSTEN, K. 1996 *Boundary layer theory*, eight edn. Springer.

SCHUBAUER, G. B. 1935 Effect of humidity in hot-wire anemometry. *Journal of research of the national bureau of standards* **15**, 575–578.

SHAPIRO, A. H. 1954 *The dynamics and thermodynamics of compressible fluid flow*. Ronald.

SMITS, A. & DUSSAUGE, J. 1996 *Turbulent Shear layers in supersonic flow*. AIP.

SMITS, A. J., HAYAKAWA, K. & MUCK, K. C. 1983 Constant temperature hot-wire anemometer practice in supersonic flows. *Exp. Fluids* **1**, 83–92.

STEINBACK, P. C. & JOHNSON, C. B. 1983 Preliminary measurements of velocity, density and total temperature fluctuations in compressible subsonic flow. *AIAA Paper* **AIAA-83-0384**, 1–18.

STEINBACK, P. C. & NAGABUSHANA, K. A. 1994 Hot-wire anemometry in subsonic slip and transonic flow regimes. *AIAA Paper* **AIAA 94-2535**.

TIJDEMAN, H. 1977 Investigation of the transonic flow around oscillating airfoils. *National Aerospace Lab. The Netherlands* **NLR TR-77-090U**.

TIJDEMAN, H. & SEEBASS, R. 1980 Transonic flow past oscillating airfoils. *Annu. Rev. Fluid Mech.* **12**, 181–222.

Tillmark, N. 2001 Private communication.